CFD SIMULATION OF NUCLEAR REACTOR FUEL SPACER ELEMENT

NÜKLEER REAKTÖR YAKIT SABİTLEME ELEMANLARININ HAD SİMÜLASYONU

REFİK KARAGÖZ

Submitted to

HACETTEPE UNIVERSITY

THE INSTITUTE FOR GRADUATE STUDIES

IN SCIENCE AND ENGINEERING

in partial fulfıllment of the requirements for the degree of

MASTER OF SCIENCE

in

NUCLEAR ENGINEERING

2008

To the Directory of the Institute for Graduate Studies in Science and Engineering,

This study has been accepted as a thesis for the degree of MASTER OF SCIENCE in NUCLEAR ENGINEERING by our Examining Committee.

Head :

_____

Assoc. Prof. Dr. Cemal Niyazi SÖKMEN

Member :

_____

Dr. Şule ERGÜN

Member :

_____

Assist. Prof Dr. İlker TARI

This is to certify that the Board of Directors of the Institute for Graduate Studies in Science and Engineering has approved this thesis on …/…/……

Prof.Dr. .....
Director
The Institute for Graduate Studies in Science and Engineering

CFD SIMULATION OF NUCLEAR REACTOR FUEL SPACER

Refik KARAGÖZ

Abstract

Fuel assemblies of LWR type nuclear reactors consist of rod bundles, arranged in a square array, and axially located spacer grids. Primarily, a spacer provides structural stability for the fuel assemblies against coolant flow. Many different types of spacer designs are present and these spacers affect fluid dynamics and heat transfer. The present study aims to investigate spacer effects on fluid dynamics and heat transfer in fuel bundles, and consists of two parts. In the first part, spacer effect on single-phase flow pressure drop, lateral and axial flow variation, and turbulence behaviour of a fuel assembly has been studied using computational fluid dynamics (CFD). FLUENT, as a commercial software was used as a CFD tool. Grid and ferrule, as the two types of spacer grids were used in the analysis. The original fuel assembly including seven axially located 8x8 grid or ferrule type spacer is reduced to a managable subchannel to get rid of high computational cost and geometric complexity. Turbulent models of k-ε, k-ω, and Reynolds Stress Model were employed to characterize the flow. In the second part, alternatively, spacer behaviour was modeled by applying porous media approach, by introducing turbulent kinetic energy, and its dissipation rate source terms to flow over a bare rod subchannel. Results obtained from the first and second parts were compared with each other and with the published scientific papers including experimental data.

Keywords: grid spacer, ferrule spacer, CFD, single-phase flow, pressure drop, lateral flow, porous media.

Advisor: Assoc. Prof. Dr. Cemal Niyazi SÖKMEN, Hacettepe University, Department of Nuclear Engineering, Nuclear Engineering section.

NÜKLEER REAKTÖR YAKIT SABİTLEME ELEMANI HAD SİMÜLASYONU

Refik KARAGÖZ

Öz

Hafif su tipi nükleer reaktör (HSR) yakıt tertibatları kare halindeki çubuk demetleri, ve eksenel olarak yerleştirilmiş sabitleme elemanlarından oluşur. Sabitleme elemanları birincil olarak yakıt tertibatına, akış karşısında yapısal kararlılık sağlarlar. Birçok farklı çeşidi bulunan sabitleme elemanları akışkan dinamikleri ve ısı iletimini de etkiler. Mevcut çalışma sabitleme elemanının yakıt demetindeki akış dinamiği ve ısı iletimine etkisini araştırmayı hedeflemekte ve iki bölümden oluşmaktadır. İlk bölümde, Hesaplamalı Akışkanlar Dinamiği (HAD) kullanarak sabitleme elemanlarının yakıt tertibatlarındaki tek fazlı akışın basınç kaybı, yanal ve eksenel değişimi, ve türbülans davranışı üzerine çalışılmıştır. Ticari HAD aracı olarak FLUENT yazılımı kullanılmıştır. Çalışmada sabitleme elemanı tiplerinden olan ızgara ve halka/farol kullanılmıştır. Yüksek hesaplama yükü ve geometrik karışıklıktan kurtulmak için, orjinal yakıt tertibatı, eksenel yönde yerleştirilmiş 8x8 ızgara veya farol tipi sabitleme elemanları, basit tek alt-kanala indirgenmiştir. Bu iki tip sabitleme elemanının bulunduğu akış özelliklerini belirlemek için k-ε, k-ω ve RSM türbülans modelleri kullanılmıştır. İkinci bölümde, alternatif olarak, sabitleme elemanı davranışını modellemek için gözenekli ortam yaklaşımı, türbülant kinetik enerji ve dağılma oranı kaynak unsurları boş çeyrek alt-kanala uygulanmıştır. Birinci ve ikinci bölümde elde edilen sonuçlar kendi aralarında ve deneysel verileri de içeren yayınlanmış bilimsel çalışmalarla karşılaştırılmıştır.

Anahtar sözcükler: ızgara, farol sabitleme elemanı, hesaplamalı akışkanlar dinamiği, tek-fazlı akış, basınç kaybı, yanal akış, gözenekli ortam.

Danışman: Doç. Dr. Cemal Niyazi SÖKMEN, Hacettepe Üniversitesi, Nükleer Enerji Mühendisligi Bölümü, Nükleer Enerji Mühendisligi Anabilim Dalı

ACKNOWLEDGMENTS

I would like to thank my advisor, Assoc. Prof. Dr. C. Niyazi SÖKMEN for his helpful guidance and endurance. I would also like to thank the committee members, Dr. Şule ERGÜN and Assist. Prof. Dr. İlker TARI for their valuable comments. I would also like to thank all members of Hacettepe University Nuclear Engineering Department, and my workfellows, and managers from Ministry of Finance, General Directorate of Public Accounts, IT Department.

CONTENTS

Page

LIST OF FIGURES

Page

LIST OF TABLES

Page

1. INTRODUCTION

1.1. Motivation

In LWR type nuclear reactor cores, fuel rods are physically supported by spacer grids located at several positions. Spacer grids, that have different types used in the industry, affect the hydrodynamics of the pressurized water and the heat transfer from the fuel rods, and this makes the spacer design crucial. The spacer grids interact with the flow and heat transfer in a number of ways. It is known that they generally have a beneficial effect on turbulence and heat transfer enhancement in typical nuclear reactor assemblies. However, the obtained enhancement depends on the geometrical characteristics of the spacer grids as well as on the parameter range in terms of pressure, and local mass velocity. Spacer grids decrease the flow cross sectional area locally and thereby increase the local pressure drop and heat transfer coefficients. Safety related design issues are important considerations in improving fuel bundle performance. Increasing the critical heat flux prevents departure from nucleate boiling and dry out. Optimizing the critical heat flux performance in the PWRs is the main focus, historically, but, as the operating conditions of the reactors have been extended through the thermal limits of the core, the single-phase heat transfer performance of the rod bundles has become an important design focus. Improvement in the single-phase heat transfer coefficients provides higher power generations. Temperature distribution on the surface of the rods is another critical consideration. The integrity of the fuel rods can be compromised if the local temperatures on the surface of the rods are too large. On one hand, larger and more uniform single-phase, local heat transfer coefficients yield increased performance, and prevent potential damage to the fuel rods which would result from areas of increased temperature. On the other hand, increasing the number of spacers throughout the reactor core causes a large pressure drop. Therefore, the optimum design and number of spacers located in the fuel assemblies lies between these two limiting conditions.

1.2. Objectives

The study consists of two parts. In the first part, subchannel analysis of spacer effect on single-phase turbulent flow and heat transfer behaviour in nuclear reactor fuel bundles were investigated. In the second part, alternatively, porous media approach, and source term modeling was applied to bare rod subchannel in order to simulate the spacer effect. The study will be accomplished by using commercially available software FLUENT. In the first part, for the two types of spacers with detailed geometry, axial and lateral development of velocity profiles, turbulent quantities such as kinetic energy, its dissipation rate, heat transfer enhancement, hot spot and temperature distribution on fuel rod surfaces, and pressure drop analysis in and downstream of spacer is recovered. Including the comparison of some results to published theoretical and experimental data, suitability of CFD models employed for each type of spacer design and relative comparison of them to each other will also be mentioned.

In the second part, alternative to the first part, source term modeling of momentum with porous media approach, turbulent kinetic energy, and its dissipation rate for related transport equations is studied in order to simulate spacer effect on the flow. The external source term models are converted to codes of some FLUENT user-defined functions (UDF). By the attachment of these UDFs to subchannel CFD calculations for bare rod bundle, model simulation is completed and compared to the results obtained from the first part.

2. CFD OVERVİEW

Modeling and simulation has been effectively used by the nuclear industry in design, management and optimization. Many of codes were developed in thermal-hydraulics area to understand the behavior for different conditions. Most of these codes were developed specifically for application to nuclear reactors and their development helped initiate and developed the field known as CFD.

With the rapid development of computing architectures CFD has evolved over the last two decades. Modern codes include full set of Navier-Stokes equations with multi-fluid and multi-phase effects. Various differencing techniques of the fundamental conservation equations are performed based on finite difference, finite volume, or finite element techniques. Special interest is focused on numerical strategies that accurately represent the differential equations, to be sure of consistency, accuracy and numerical stability in the solution. The obtained group of algebraic equations may be solved by direct or iterative matrix solvers. Most commercial codes use iterative approaches, such as incomplete LU decomposition, alternating direction (ADI) methods, conjugate gradient methods, multigrid methods, etc. are employed [WEBER, 1999].

2.1. Modeling Turbulence

The nature of turbulence generally leads to analysis of the Navier-Stokes equations in some average sense. Most often, they are called as Reynolds Averaged Navier-Stokes equations (RANS), when the flow field variables are split into a mean and fluctuating component. The resulting mean flow equations then contain terms representing turbulence interactions, presenting the so-called turbulence closure problem. When these terms are modeled in terms of the mean flow variables, such as in the Boussinesq and k-ε approaches, a complete set of equations can be determined. This is the common approach in commercial CFD codes.

The solution variables in the exact Navier-Stokes equations are decomposed into the mean (ensemble-averaged or time-averaged) and fluctuating components, in the Reynolds averaging approach. For the velocity components:

$$u_i = \overline{u}_i + u_i' \tag{2.1}$$

where $\overline{u}_i$ and u_i' are the mean and fluctuating velocity components (i = 1, 2, 3).

Substituting expressions of this form for the flow variables into the instantaneous continuity and momentum equations and taking a time (or ensemble) average (and

dropping the overbar on the mean velocity, $\overline{u_i}$) yields the ensemble-averaged or Reynolds-averaged Navier-Stokes (RANS) momentum equations. They can be written in Cartesian tensor form as:

$$\frac{\partial \rho}{\partial t} + \frac{\partial}{\partial x_i}\left(\rho u_i\right) = 0 \tag{2.2}$$

$$\begin{aligned} \frac{\partial}{\partial t}\left(\rho u_i\right) + \frac{\partial}{\partial x_j}\left(\rho u_i u_j\right) = \\ -\frac{\partial p}{\partial x_i} + \frac{\partial}{\partial x_j}\left[\mu\left(\frac{\partial u_i}{\partial x_j} + \frac{\partial u_j}{\partial x_i} - \frac{2}{3}\delta_{ij}\frac{\partial u_l}{\partial x_l}\right)\right] + \frac{\partial}{\partial x_j}\left(-\rho\overline{u_i' u_j'}\right) \end{aligned} \tag{2.3}$$

The equations have the same general form as the instantaneous Navier-Stokes equations, with the velocities and other solution variables now representing ensemble-averaged (or time-averaged) values. Additional terms now appear that represent the effects of turbulence. These Reynolds stresses, $-\rho\overline{u_i' u_j'}$, must be modeled in order to close Equation 2.3. A common method employs the Boussinesq hypothesis [Hinze, 1975] to relate the Reynolds stresses to the mean velocity gradients:

$$-\rho\overline{u_i' u_j'} = \mu_t\left(\frac{\partial u_i}{\partial x_j} + \frac{\partial u_j}{\partial x_i}\right) - \frac{2}{3}\left(\rho k + \mu_t \frac{\partial u_i}{\partial x_i}\right)\delta_{ij} \tag{2.4}$$

The Boussinesq hypothesis is used in the Spalart-Allmaras model, the k-ε models, and the k-ω models. The advantage of this approach is the relatively low cost associated with the computation of the turbulent viscosity, μ_t. In the case of the Spalart-Allmaras model, only one additional transport equation (representing turbulent viscosity) is solved. In the case of the k-ε and k-ω models, two additional transport equations (for the turbulence kinetic energy, k, and either the turbulence dissipation rate, ε, or the specific dissipation rate, ω) are solved, and μt is computed as a function of k and ε. The disadvantage of the Boussinesq hypothesis as presented is that it assumes μt is an isotropic scalar quantity, which is not strictly true. The alternative approach, embodied in the RSM, is to solve transport equations for each of the terms

in the Reynolds stress tensor. An additional scale-determining equation (normally for ε) is also required. This means that five additional transport equations are required in 2D flows and seven additional transport equations must be solved in 3D. In many cases, models based on the Boussinesq hypothesis perform very well, and the additional computational expense of the RSM is not justified. However, the RSM is clearly superior for situations in which the anisotropy of turbulence has a dominant effect on the mean flow. Such cases include highly swirling flows and stress driven secondary flows [FLUENT ug, 2006].

The CFD code used in this study, FLUENT, provides the following turbulence models:

- Spalart-Allmaras model
- k-ε models
    - Standard k-ε model
    - Renormalization-group (RNG) k-ε model
    - Realizable k-ε model
- k-ω Models
    - Standard k-ω model
    - Shear-stress transport (SST) k-ω model
- v^2-f model
- Reynolds stress model (RSM)
- Large eddy simulation (LES) model

The detailed information about these models can be found in Appendix-A, and in Fluent User guide [FLUENT ug, 2006].

2.5. Background

Thermal-hydraulic analyses have been performed to insure that the reactor core and coolant, control and protection systems have appropriate margins to ensure that specified acceptable fuel design limits are not exceeded during any condition of normal operation, including the effects of anticipated operational occurrence. While

experimental studies have been carried out to provide these assurances, with the quick development of computation technologies, CFD tools were developed and used in design and operational analysis. Lots of studies have been accomplished in order to validate these tools and improve CFD capabilities, and technologies. Below, a few of general studies on in-core nuclear reactor studies informing the state of this field are given.

Gango (1997) studied mixing in subchannels in parts of the VVER-440 fuel assembly by using the FLUENT/UNS computer code. Three geometries are reported including 30°of the bundle cross-section with corner section and without spacers (144 045 cells), 30°of the bundle cross-section with corner region and spacers (306 936 cells), and 60°of the bundle cross-section including the corner region and with two spacers positioning modeled in detail (316 110 cells).

Different fuel heat flux for the rods was applied with axial power profile. Standard k-ε model with wall function was used with second order discretization schemes and temperature-dependent physical properties of coolant. The level of mixing was characterized by means of parameter $(T_{isol} – T)/T_{isol}$ for the hot subchannel. Here, T_{isol} and T are subchannel-averaged temperatures for isolated subchannel (no mixing) and hot subchannel of the present study. Axial developments of the hot subchannel average temperature and the assembly pressure drop are shown. The spacers increased the level of mixing by about 100%.

By Creer et al (1976), experiments were performed at Pacific Northwest Laboratories to investigate turbulent flow characteristics in a 7 x 7 fuel rod bundle consisting of 0.996-cm-diameter rods with a pitch of 1.369cm. Laser Doppler anemometer was used to measure axial local mean velocity and local turbulence intensity. Water was the working fluid with at 29.4°C with Reynolds Numbers of 14000, 29000, and 58000. The study was then declared as benchmark. Then Tzanos (2001, 2001a, 2002) studied on predictive power of several turbulence models. In Tzanos (2001), standard high-Reynolds k–ε model, k–ε model with non-linear stress-strain vorticity relations, and low Re-number k–ε model were compared to experimental data of Creer et al. (1976). One eight of a bundle 7 x 7 fuel rods was modeled based on an unstructured

grid with 164000 cells for high-Re models and 320000 cells for low-Re model. All k–ε models produced nearly the same results. They over predicted the velocity around the centre of the flow channel and under predicted it in the gaps between the 7 rods. The models over predicted the turbulence in the area of the gaps. Similar conclusion was expressed in Tzanos (2002), where RNG k – ε model and another low-Re k–ε model were tested in one subchannel of the 7 x 7 bundle. The Smagorinsky LES model was tested in Tzanos (2001a). Two neighboring subchannels were selected as computation domain with 616000 cells. It is reported “the LES simulation of flows in LWR fuel bundles is superior to that of k–ε models and the LES may provide a quite faithful simulation of these flows”.

Weber et al. (1999, 2001) studied on thermal-hydraulic analysis of reactor core by using commercial software CFX and STAR-CD. The comparison of velocity and temperature fields in reactor cores with different software was aimed. Analysis for the hot assembly, analysis of the hot assembly with its closest neighbors for hot rod, and analysis of a part of the hot assembly with hot rod giving DNBR were performed with VIPRE subchannel analysis code, and with CFD codes CFX and/or STAR-CD. In the analysis of the hot rod, the one-quarter of the subchannel defined in the square arrangement as the region between four fuel rods was analyzed with both VIPRE and CFX codes. The CFX mesh contained 268 984 cells, the inlet velocity and temperature were prescribed. Temperature dependent specific heat and density of water were used. The cross-section averaged temperatures and velocities in both computations were in close agreement. In the analysis of hot assembly, VIPRE and STAR-CD codes were applied. One quarter of an assembly containing 8 x 8 bare fuel rods was selected. Two mesh configuration were used, of one had 473600 cells, and the second had 3765600 cells. The cross-sectional average velocities and temperatures were again similar for both codes and both meshes. In the analysis of one-eight core region, the STAR-CD model had 57400800 mesh cells.

Weber et al. (2001), analyses of one-eight of the core with spacer grid/mixing vane structures were performed with VIPRE and STAR-CD. The spacer grid or mixing vanes were modeled and additional porous media approach was used. In the porous

media study, 68019948 cells, and in the other geometry, 240222348 computational cells were configured. The spacer and mixing vanes were treated as infinite thin surfaces and only a selected length of the assembly around the spacer was taken into account. The number of cells was approximately 250000 and grid sensitivity was checked in one case. Inlet boundary conditions were taken from a computation without spacers and pressure boundary condition was adopted at the outlet. The other boundaries except of walls were treated as periodic. Hybrid differencing was used with standard k–ε model of turbulence. The CFX predictions were compared for one type of the vane with experimental results of Karoutas et al. (1995) and Yang, Chung (1998).

Conner, Smith (2002) applied a CFD code to simulation of the effect of swirling vanes. Two neighboring subchannels in a square array of 5x5 rod bundle was studied by STAR-CD code using periodic boundary in the gaps, RNG k–ε turbulence model and realistic geometry of the grid and vanes. In the experiment with working fluid as water, lateral velocity vectors and average heat transfer coefficients were measured. Comparison of computations and measurements revealed good agreement for various parameters such as maximum lateral velocity magnitudes downstream of the grid (within ±10%), pressure drop across a grid span (within ±2%), turbulent intensity just upstream of next grid, and average heat transfer coefficient as a function of downstream of the grid (within ±11%).

Aszódi, Légrádi (2002) used CFX code for the analysis of coolant mixing in VVER-440 reactor fuel assemblies. Rod bundle representing 60-degree of a fuel assembly cross section contained 24 fuel rods and a spacer grid. Hybrid mesh with 2000000 unstructured and 350000 structured control volumes represented fuel bundle. The model of fuel assembly head consists of the flow domain above the fuel rods, the mixing grid, the hole of the bottom plane of the reactor lower plenum, and the thermocouple positioned above it. The k-ω model of turbulence was used. Fully developed flow in rod bundle was calculated using periodic boundary conditions. The analyses mentioned so far dealt with single-phase flows only and in fact the DNBR was one of the important outputs.

In 2005, series of studies were carried out for high resolution and full-scale experimental data, on a sub-channel basis, under actual operating conditions of BWRs by Pennsylvania State University (PSU), USA and Japan Nuclear Energy Safety (JNES) Organization, in cooperation with OECD/NEA and Commissariat á l'Energie Atomique (CEA). A multi-rod assembly with a typical reactor power and fluid conditions were measured in the NUPEC BWR BFBT facility, which was able to simulate the high-pressure, high temperature fluid conditions found in nuclear reactors. An electrically-heated rod bundle was used to simulate a full scale reactor fuel assembly. De-mineralized water was used as a cooling fluid. The maximum operating conditions for the facility were 10.3 MPa in pressure, 315 °C in temperature, 12 MW in test power, and 75t/h in flow rate. The pressure drop was measured in both single-phase flow conditions that cover the normal operational behavior. Many benchmark cases including single-phase steady-state pressure drop, were declared for comparison of currently available computational approaches.

3. CFD STUDY

The effect of structural supporting elements of nuclear reactor fuel assemblies, spacers, on the fluid dynamics and heat transfer is investigated by using CFD for two types of spacers, grid and ferrule, as declared in BFBT benchmark. Subchannel approach is employed to model turbulent and heat transfer characteristics of flow. Details of the model, computational domain and mesh, convergence of solutions, and turbulence modeling are discussed.

3.1. Model and Simulation Details

The computational simulations model the fluid dynamics and heat transfer for the flow of water through the subchannel with a Reynolds number of approximately 240000 to match one of the cases defined in the BFBT experiment measurements. Two types of spacers, grid and ferrule, as schematically given in Figure 3.1 and Figure 3.2 [OECD/NRC Benchmark, 2004], are modeled. The flow in the subchannel is single-phase, turbulent, incompressible and three-dimensional. The working fluid, water, is modeled using a constant density of 762 kg/m^3, constant specific heat of 4.184kj/kg-

K. In addition, thermal conductivity and dynamic viscosity are independent of temperature. Only steady state computational solutions are studied.

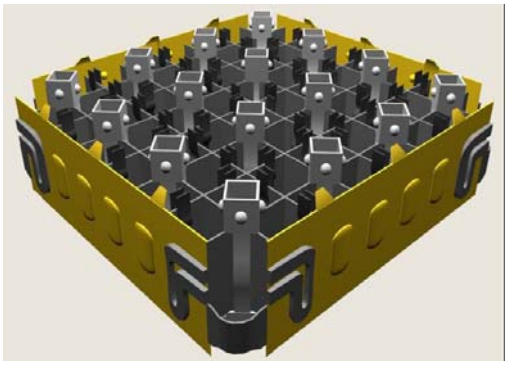

Figure 3.1 : Grid Spacer.

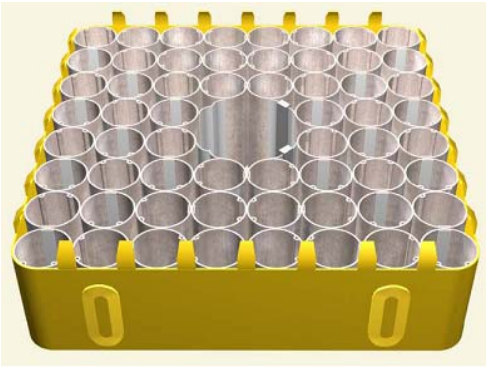

Figure 3.2 : Ferrule Spacer.

The steady-state form of the Reynolds-Averaged Navier-Stokes continuity, turbulence, and energy equations are discretized and solved by using FLUENT software, release 6.2.16. k-ε, k-ω, and RSM turbulence closure models with and without enhanced wall treatment options are investigated in the present study. A segregated, implicit solver is used to solve the governing equations. First-order upwind discretization schemes for the convective terms in the momentum, energy, and turbulence parameters are employed. In addition, the SIMPLE pressure-velocity coupling is implemented.

3.2. Geometry and Meshing

Detailed geometric models in order to incorporate as many characteristics of the physical geometry as are possible for the two types of spacers has been used. Only extremely small geometric details are oversimplified. In the experimental setup prepared by BFBT, seven of 8x8 spacers are placed axially along the fuel rod assembly. The smallest repeating structures, being just one spacer in axial direction and a quarter or one subchannel in lateral direction, are used in the numerical studies. A single periodic structure for the grid type spacer is given in Figure 3.3.

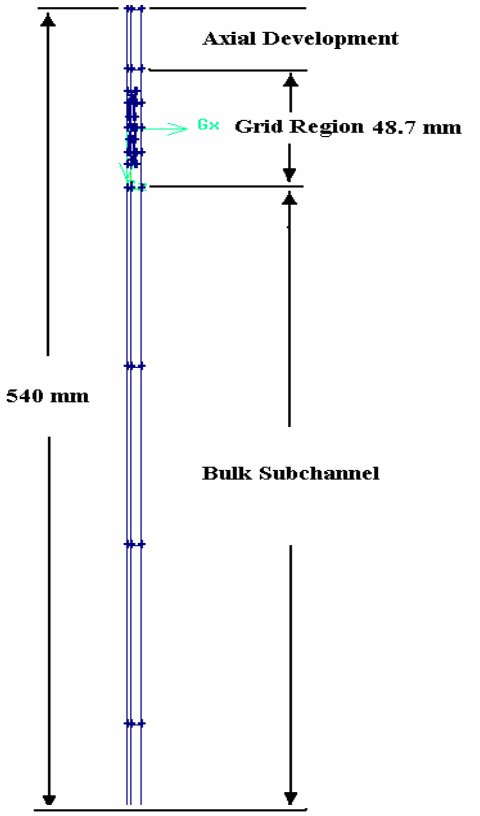

Figure 3.3 : Single periodic structure for grid spacer.

The two subchannel domains are representative of an infinite array rod bundle: therefore wall effects are not captured in the computational model. As seen from the Figure 3.3, an axial development, a spacer region and a bare rod region must be represented. The grid and ferrule type spacers are located at the origin of the domain and axially lie between ±1.64 and ~1D_h, respectively. Indeed, the dimensions of the bare rod region had been extended in order to reach a point where all variable gradients disappear (~30D_h). Similar experimental studies show that the flow is fully-developed by approximately 30 to 40D_h downstream of the support grid; thus, fully developed or nearly fully-developed flow is expected at the end of the computational domain.[Karoutas et al., Yang and Chung, 1998] In these cases, the overall length of the subchannels, axial sum of the axial development region, spacer and bare rod region length, are 37.3D_h and 36.5D_h for the grid and ferrule type spacers, respectively.

The ferrule-type spacer is modeled as one sub-channel, interior region of four fuel rods, while the grid-type as a quarter of one sub-channel. Figure 3.4 and Figure 3.5 show the subchannel approach with the spacers depicted, of grid and ferrule type spacers, respectively, and Figure 3.6 and Figure 3.7 show different 3-D views of the two types of spacers.

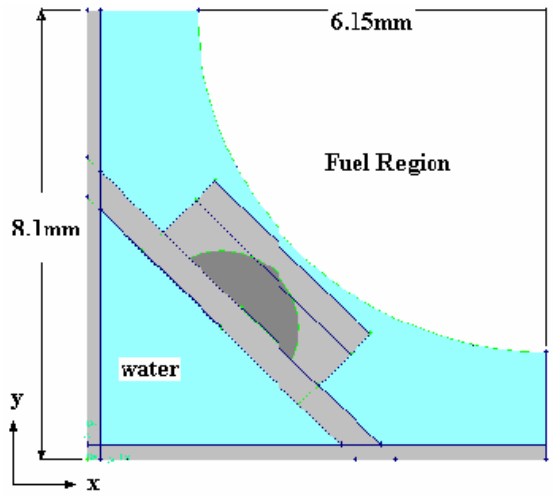

Figure 3.4 Lateral view of Grid spacer

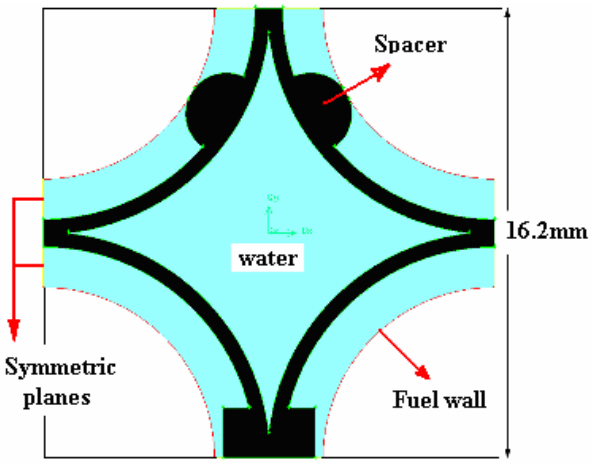

Figure 3.5 Lateral view of Ferrule Spacer

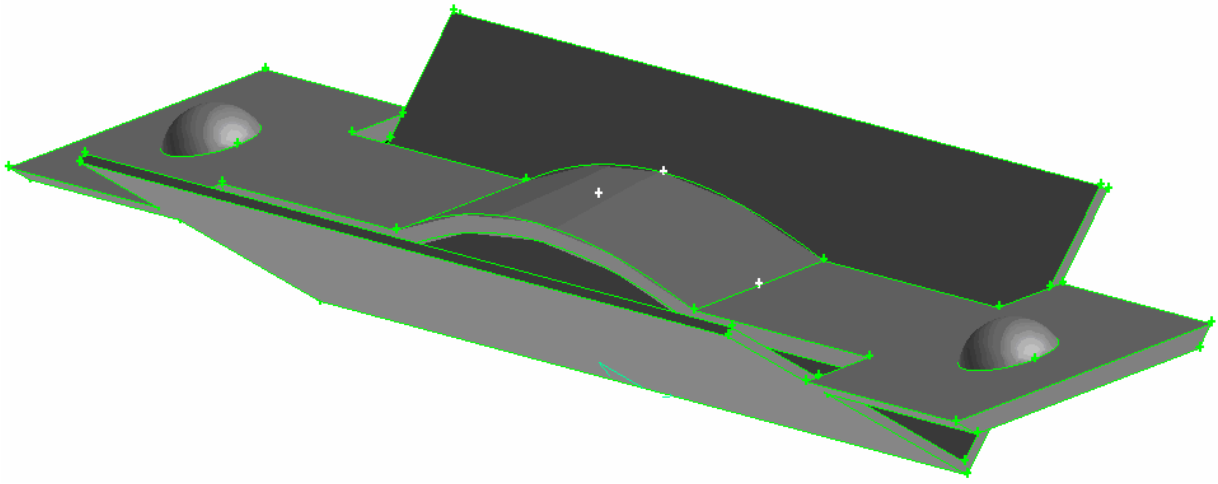

Figure 3.6 : A 3-D modeled view of grid spacer.

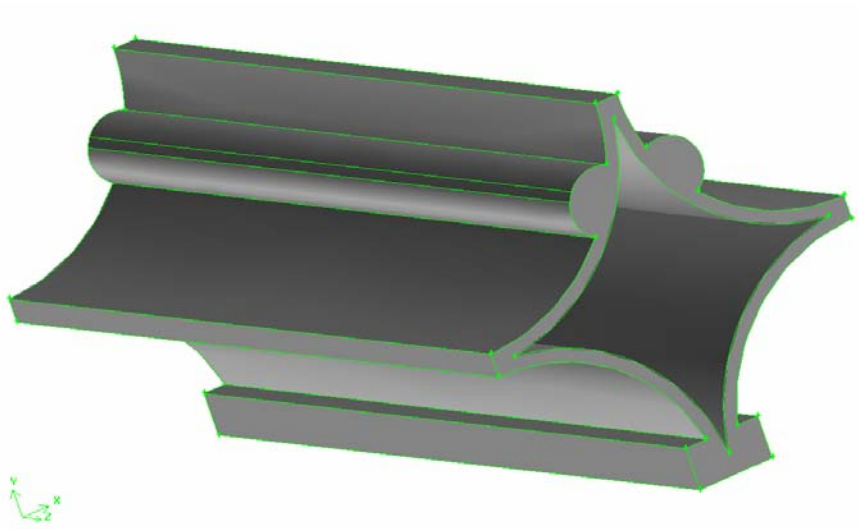

Figure 3.7 : A 3-D modeled view of ferrule spacer.

Small simplifications were applied to geometries in order to get rid of high mesh density, and computational cost. In grid spacer, touching point between spacer and fuel was separated resulting in a very small distance. In ferrule spacer, the touching line between spacer and fuel wall was intersected which resulted in a small area. Furthermore, at the inner part of the ferrule spacer, sharply intersected lines of the cylindrical surfaces were simplified by increasing the radius of cylindrical geometry by 2-3 percent.

The mesh was applied to these geometries using commercially available software GAMBIT, version 2.2.30. Tetrahedral/Hybrid elements with T-grid approach was used in constructing meshes. Mesh size function capability of the software was employed for resolving sharp-edged zones in the spacer region. At first, spacer region is meshed by separating the whole spacer domain into small pieces, since the difficulty in meshing sharp-edged zones and outer open regions with only one operational step and to be able to capture the near-wall region resolution well, and then mesh on the boundaries was extended through inlet and outlet of the bulk subchannel regions by increasing the cell sizes step by step. Nearly 1000000 cells for the ferrule-type, and 550000 cells for the grid-type geometry, were created. The flowing water volume is 19 cm^3 for the computational domain with grid geometry and 73 cm^3 with ferrule geometry. A view of the grid-type spacer mesh is given in Figure 3.8.

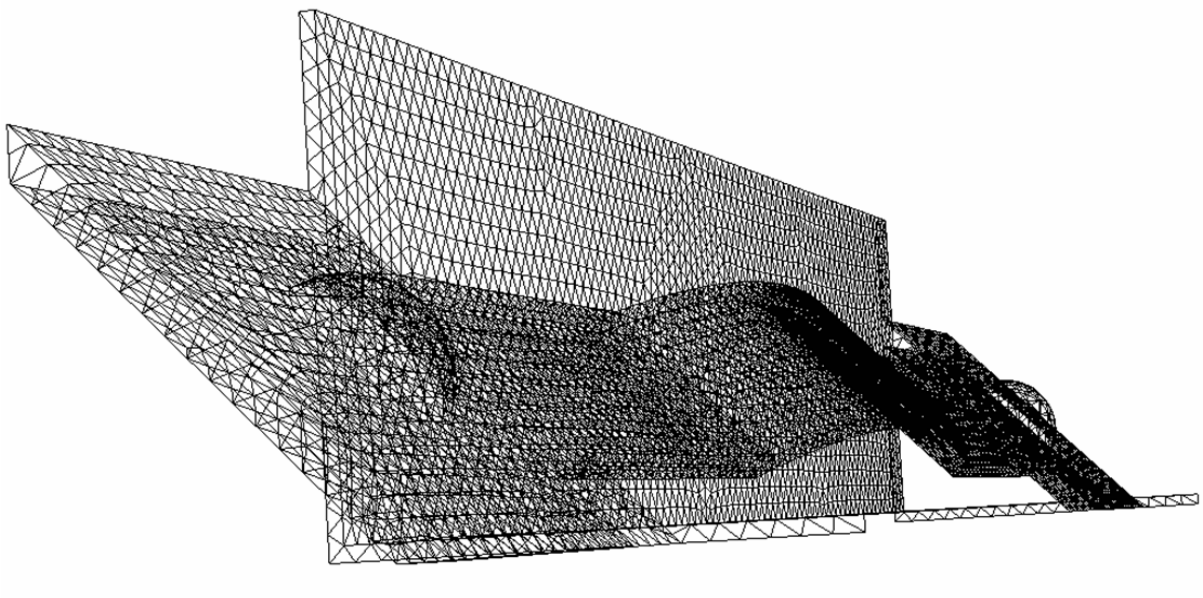

Figure 3.8 : A meshed view of grid-type spacer.

3.3. Boundary Conditions

The boundary conditions consist of a velocity inlet, pressure outlet, and symmetry plane for the water interfaces. Initially, a fully developed velocity profile was obtained by a FLUENT run for the bare rod region, that is 160mm long and without a spacer. Then its output, such as axial velocity, turbulent kinetic energy, and its dissipation rate profiles, was applied to original geometry's velocity inlet boundary condition. The final length of the computational domain, that is the pressure outlet axial location, was determined iteratively extending the bare rod region length by observing the parameter variations, such as vorticity magnitude, and velocity gradients at each iteration. For the fuel and spacer walls, no-slip condition was defined. Typical PWR fuel and coolant thermal conditions were applied. 557K is specified as coolant temperature at the inlet of subchannel, in the velocity inlet boundary condition, and a constant 200kW/m^2 heat flux is specified for the fuel wall heat flux.

From the BFBT experimental data, 55t/h mass flow rate of coolant is chosen, for the operational conditions specified for the numerical solution. This mass flow rate was resulted in a constant velocity magnitudes for the inlet of 2.1m/s. For the pressure

outlet boundary condition, 7.15 MPa was specified as in the case of BFBT and applied.

3.4. Cases Investigated

Turbulent models of RSM, standard k-ε, and standard k-ω in FLUENT software were employed for each of the spacer types. The models investigated in the present study are in the Reynolds-averaged group and they are accepted as practical engineering calculation methods. In the standard k-ε model, transport equations for the turbulence kinetic energy, k, and turbulence dissipation rate, ε, are solved in addition to continuity, momentum, and energy equations. The RSM model solves the transport equation and an additional equation for the turbulence dissipation rate. The linear pressure-strain model with the included reflection-term is used. Additionally, k-ε and k-ω models are isotropic based on the Boussinesq approach, whereas RSM model incorporates anisotropy of the Reynolds stresses.

In turbulence modeling, near-wall treatment is an important consideration. In all the models employed in the present study, both standard and enhanced wall treatment options are used although wall average y^+ values for each of the grid configurations range between 12 to 17.5

Table 3.1. Cases investigated

Case#	type	length(mm)	cells	turb. model	wall treatment
case-1	grid	540	529406	k-ε Standard	enhanced
case-2	grid	540	529406	k-ε Standard	standard
case-3	grid	540	529406	k-ω Standard	enhanced
case-4	grid	540	529406	k-ω Standard	standard
case-5	grid	540	529406	RSM	standard
case-6	grid	540	529406	RSM	enhanced
case-7	ferrule	515	987479	k-ω Standard	standard
case-8	ferrule	515	987479	k-ω Standard	enhanced
case-9	ferrule	515	987479	k-ε Standard	enhanced
case-10	ferrule	515	987479	k-ε Standard	standard
case-11	ferrule	515	987479	RSM	enhanced
case-12	ferrule	515	987479	RSM	standard

Totally 12 cases including various configurations for both grid and ferrule-type spacer were documented including analysis of lateral (secondary) flows, axial development, pressure drop, heat transfer, comparison of turbulent models and grid design. The cases are given in Table 3.1.

3.5. Solution and Convergence

The modeled cases were solved using FLUENT software. A segregated, implicit solver option was used to solve governing equations. First order upwind discrimination scheme for the terms in the momentum, energy, and turbulence parameters were employed. A standard pressure interpolation scheme and SIMPLE pressure-velocity coupling was implemented.

The convergence of the solutions were determined by monitoring the behavior of one of the most difficultly converging parameters, such as x, y, and z component of the vorticity at a location where flow is rather complex. The solver is stopped when all the monitored variables does not change with increasing iterations. With this approach, convergence criterions corresponded to between 5.10^{-3} to 10^{-5}, and iteration numbers between 350 to 2000(case-6). Actually, the convergence of the solutions that had been applied an initial fully developed axial velocity, turbulence kinetic energy, and dissipation rate profiles to the inlet of the computational domain were easier than the trial ones which have constant inlet profiles. An exemplary scaled residual and a monitored variable plots for case-4 are given in Figure 3.9 and Figure 3.10, respectively.

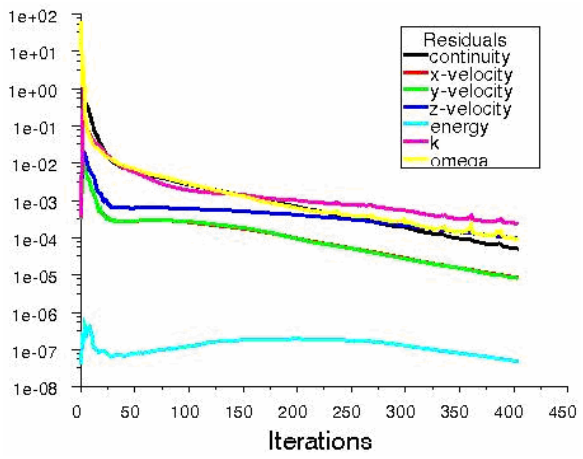

Figure 3.9. Convergence history of scaled residuals (case-4).

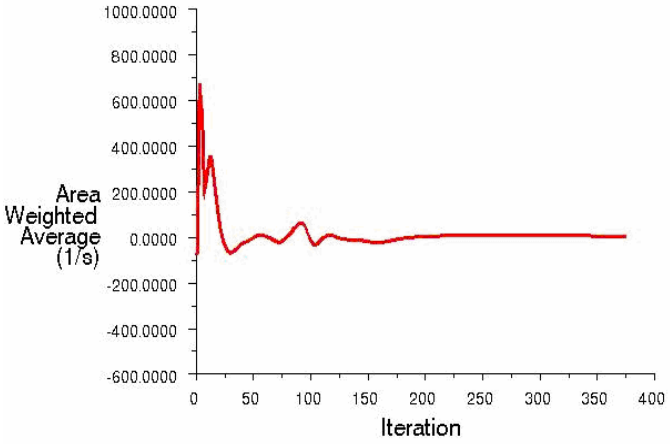

Figure 3.10. Convergence history of monitored variable, x-vorticity (case-4).

4. RESULTS

CFD for the flow dynamics and heat transfer characteristics in and downstream of spacer were performed with a Reynolds number of 240000, for the two types of spacers, grid and ferrule. As specified in BFBT benchmark, two computational domains for each of the spacer type were configured. Both subchannels are representative of the infinite array rod bundle implemented by using the smallest repetitive structure and applying symmetrical boundary conditions, as mentioned in Section 3.3. For ferrule type spacer computational domain consisted of an interior region of four square-array fuel rods, while for grid spacer it is a corner shaped,

quarter of ferrule spacer, subchannel. Spacer effect on single-phase pressure drop, lateral and axial flow development, turbulent behaviour, and heat transfer has been analyzed. Different views of the subchannel structures can be seen in Figure 3.3 – 3.5.

4.1. Lateral Flows

Lateral or secondary flows are defined as the flows directed normal to the direction of the main flow and resulted from the excessive turbulence effect of walls which causes the flow directed to open areas. A typical lateral velocity vector profile of grid type at 1.5 hydraulic diameter (D_h) downstream of spacer is given in Figure 4.1. General characteristics of the flow field are representative of the other runs. As can be seen from the figure, there are swirling flow structures present in the subchannel. The rotational sense of the vortices is consistent with each other. Separation regions are identified in the figure.

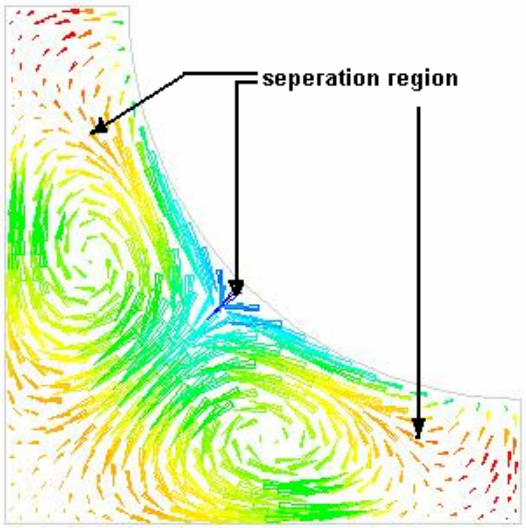

Figure 4.1 Example, grid spacer lateral velocity vector profile.

4.1.1. Axial Variation of Lateral Flows in Spacer Region

Lateral flow analysis in spacer region were accomplished. For grid type spacer, the ratio of maximum lateral velocity to average axial velocity ranged from 22 to 30%. This partially enhances the heat transfer capability from fuel surface to fluid. Identical lateral velocity profiles were obtained. However, no swirling fields were obtained in ferrule type spacer, except of lateral flows at the spacer inlet and exit. Therefore, no lateral analysis for ferrule type spacer were performed.

Grid spacer, extends from -1.64D_h mm to +1.64D_h mm, totally 3.28D_h mm in axial direction. Lateral velocity vector profiles in spacer region, for case-1, 3, 6, all with a scale factor of 50, at different axial locations of -1, -0.5, 0, 0.5, 1,and 1.6D_h are given in Appendix-B. The coloration is scaled with velocity magnitude. The sample points are also shown in figure 4.2.

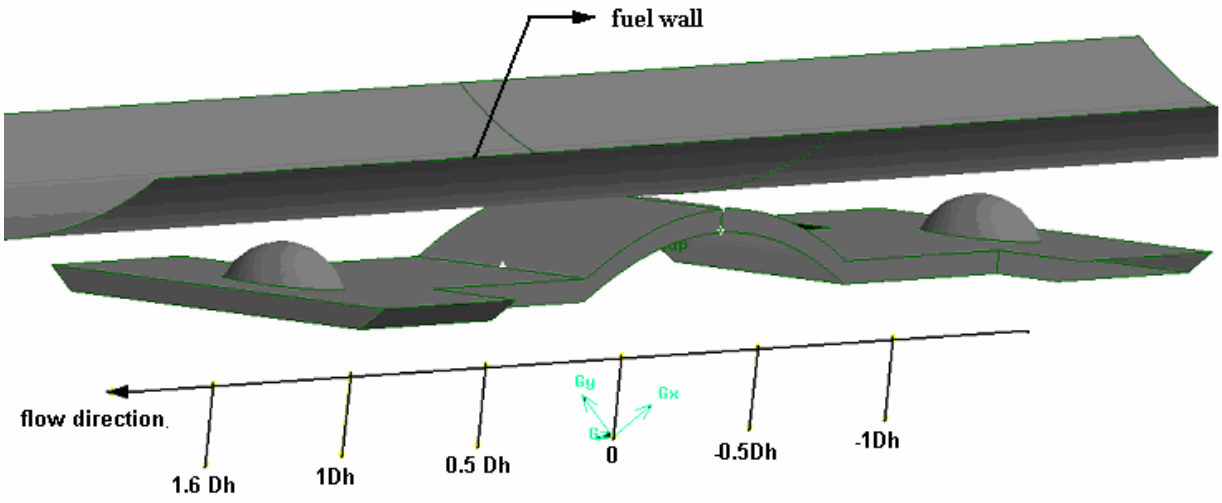

Figure 4.2. Axial sample locations of lateral velocity profiles for grid spacer.

As represented in Figure 4.2, for the first axial half of the spacer, as flow enters into the spacer, it firstly faces the rectangular structure with a semi-sphere on each side, and then there is a humpback that touches and provides structural support to fuel. Local lateral velocity fields are formed at the beginning of the spacer as the result of the entrance region and semi-spheres, but the primary swirling lateral velocity fields begin to develop when the flow progresses through the space between humpback

and fuel wall. Flow escapes to other side of the humpback, to the central region of the subchannel, from the lateral sides. The reverse processes is valid for the second half of the spacer.

The greatest lateral vector magnitudes over whole computational domain developed in the spacer region. The ratio of facet-maximum lateral velocity to average axial velocity over a plane reaches at a value of 30%. This makes the lateral velocity analysis necessary. In-spacer lateral velocity patterns are nearly the same for all the cases. As seen from the lateral velocity vector figures, fluid begins to escape from fuel-wall-side to center of the subchannel at axial location of $-1D_h$, and swirling fields appear at axial location of $-0.5D_h$. Separation originates from the middle of the humpback and impingements can be seen to fuel wall and spacer. At axial center of the spacer, 0-plane, two vortices under the humpback part of the spacer are captured and can be seen in the given figures. Progressing further into the spacer through $0.5D_h$, these vortices are shifting to upper side of the spacer blade, again between spacer and fuel wall. The vortices can be seen weakly at $1D_h$ and disappears before exit.

4.1.2. Axial Variation of Lateral Flows Downstream of Spacer

The axial variation of the lateral flow structures downstream of grid and ferrule type spacer are given in Appendix-C. Although, axial velocity is clearly dominant in these spacer designs, lateral flows were analyzed in after-spacer region or downstream of spacer to understand general behavior. Lateral velocity vector plots at axial locations of 1.5, and $3D_h$ for grid spacer, 3 and $7.5D_h$ for ferrule spacer are included in the figures. Sample locations were chosen due to visualizations of lateral flows. For grid and ferrule type spacers, a vector scale factor of 800 was used. The coloration is scaled with velocity magnitude. At axial locations of 1.5, and $3D_h$ for grid type spacer profiles, two vortices with clockwise and counter-clockwise rotational sense can be seen in the subchannels, except of case-3, which has additional two small vortices. At axial location of 1.5 D_h, the center locations of circular-shaped vortices for case-1, 2,

5, and 6 are very close to each other, while they are shifted through symmetry lines with elliptical shapes rather than circular ones, as in case-4.

4.1.2.1 Grid spacer

As mentioned above, one mesh configuration was used for the grid type spacer runs. As can be seen from the lateral velocity vector profiles, in Appendix-C, near wall resolution of cases 1, 2, 3, and 5 are fine while cases 4, 6 are not captured well. For case-1, and case-2, that are both standard k-ε model with enhanced and standard wall treatment, results are fine and very close to each other. However, near wall solution with enhanced wall treatment, case-3, in FLUENT terminology it is transitional flow option checked, is better than the one with standard wall treatment, case-4. For the RSM models, solution with standard wall treatment, case-5, gave better results than the solution with enhanced wall treatment, case-6.

After axial location of 5 D_h, swirling structures downstream of spacer in case-1, and case-4 are disappeared. However, they are seen neatly even at axial location of 10-15 D_h for case-3 and case-5. The swirling structure penetration in case-2 and case-6 are at intermediate level of the two above, which are disappeared at axial location of about 7.5 D_h.

4.1.2.2. Ferrule Spacer

A typical lateral velocity vector profile of ferrule spacer type at 1.5 hydraulic diameter (D_h) downstream of spacer is given in Figure 4.3. Two small vortices with clockwise and counter-clockwise sense can be seen at the top of the subchannel. For the ferrule type spacer results, nearly, there is not any symmetrical lateral velocity vector profile obtained. As well as for the grid type spacer, axial velocity is very dominant, that is, lateral flows are quite weak. Near-wall resolution of velocity gradients are fine enough for cases except of the RSM runs, case-11, and case-12.

In all cases of the ferrule type spacer lateral vector profiles, a scale factor of 800 was used. As can be seen from the lateral velocity vector profiles, in general, there is no symmetrical swirling structures contrary to the case of grid type spacer. Even in case-

9, there is not any swirling structure. In case-7 up to axial location of 5 D_h, there are three non-symmetrical recirculating structures, while in case-8 there are five up to 7.5 D_h, and in case-10 there are three of them up to 3 D_h. After these locations, recirculation zones disappear. There are two small vortices at the top of the subchannel up to axial location of 3 D_h, and then a randomly oriented vectoral pattern takes place, in case-12. Although near wall resolution is the worst of all, it can be said that the most symmetrical vectoral pattern can be seen in case-11. At 1.5 D_h, there are two small vortices at the top of the subchannel, that is in the page plane, which are shifted through bottom at 5 D_h, and two vortices at each direction, totally eight ones taking place in the subchannel was observed even up to axial location of 15 D_h. Additionally, near wall solutions of case-11, and case-12 are not resolved enough, while the others are satisfactory.

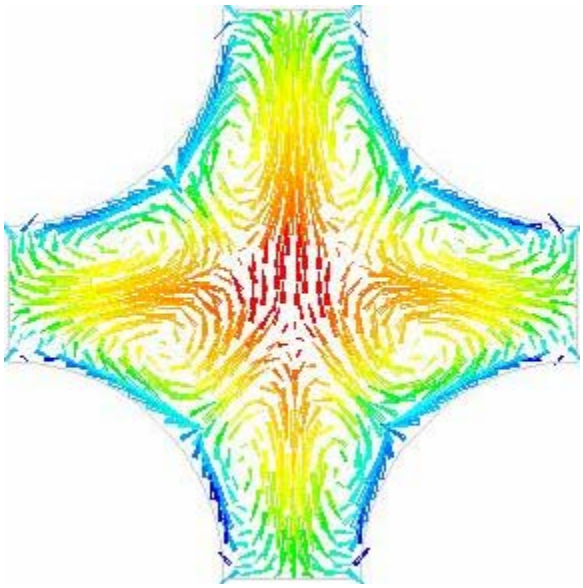

Figure 4.3. Example, ferrule spacer lateral velocity vector profile.

4.2. Axial velocity and turbulent kinetic energy variation

Detailed study must be carried out in order to understand the nature of the flow by analyzing the velocity magnitude and turbulent kinetic energy contours, but an overview of these quantities along entire subchannel would be a beneficial introduction to see effects of supporting spacers.

4.2.1. Grid Spacer

As discussed in the boundary conditions section, in order to apply fully developed profiles to the inlet of the subchannels, bare rod subchannel configurations were prepared. For the grid type spacer, a 120mm-long bulk subchannels were run for the cases from 1 to 6. The outlet plane profiles of axial velocity, turbulent kinetic energy, and turbulent dissipation rate were obtained. These profiles have been used as the inlet boundary conditions of the cases.

Velocity magnitude and turbulent kinetic energy plots averaged in some particular x-y planes, and also along a nearly central line over entire subchannel are given in Figures 4.4 to 4.7. As seen from the velocity magnitude plots, velocity magnitude shape over spacer region, that is from -24.35 to 24.35 in z-direction, is typically the same for all cases. Maximum value of velocity magnitudes range from 3.2 to 3.5 m/s, and reached at the center of spacer, z=0. After spacer region, for plot over central line, velocity graphs differ from each other in some way. For cases 1, 2, and 6 graph shapes are similar, that is, velocity magnitude value increases and reaches at a constant value of ~2.4 m/s at different axial locations. However, velocity magnitude of case-3 and case-5 increases through bare rod region and have a peak value of 2.7 m/s at axial location of 22 D_h downstream of spacer. In case-4, with a different shape, velocity magnitude peaks at axial location of 4 D_h downstream of spacer and reaches at a steady value of 2.2m/s.

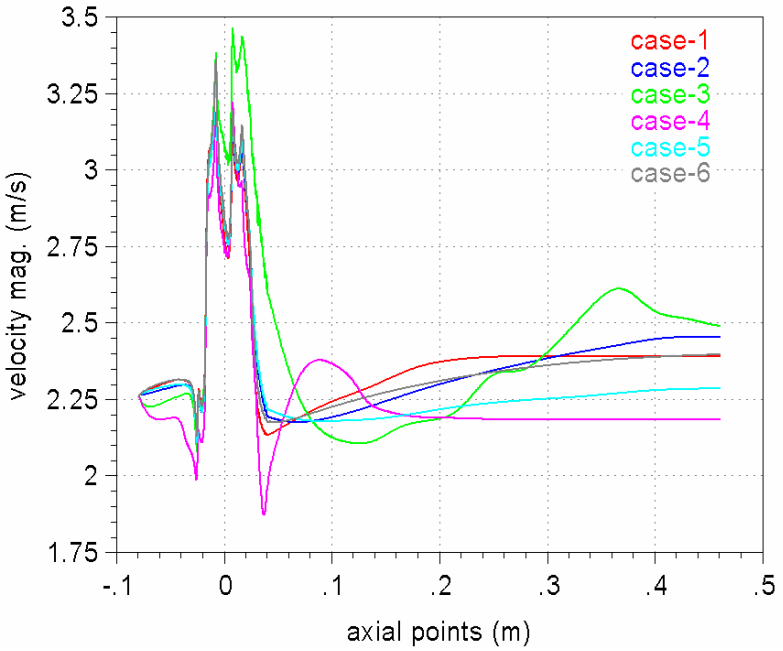

Figure 4.4. Axial variation of velocity magnitude over central line: grid spacer.

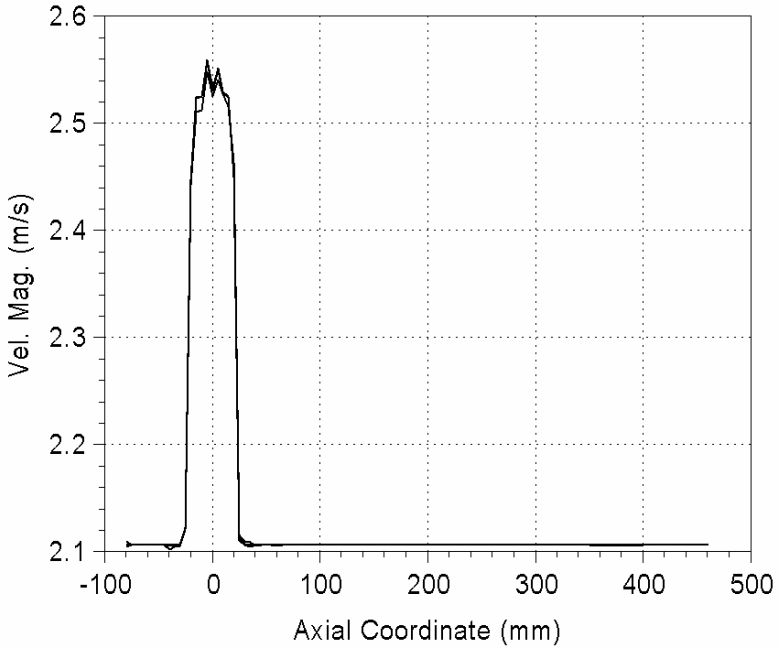

Figure 4.5. Axial variation of averaged velocity magnitude: grid spacer.

As can be seen from the turbulent kinetic energy plots, spacer region caused turbulence production as expected. The nature of this phenomena, in general,

consisted of an increase in turbulent kinetic energy at inlet of spacer and had a local maxima in the middle, where flow area is partially extended, and tends to be decreased while passing the spacer exit. At the exit of the spacer region, for cases-1, 2, 3, and 6, turbulent kinetic energy curves had a local minimum, and after exiting the spacer, again a local maxima point at axial location of 1 to 3 D_h can be seen. As flow progresses into the subchannel, these curves tend to reach at some constant values. For case-4, turbulent kinetic energy curve has a maximum in spacer region as well as others and after exiting the spacer region had its minimum value of nearly equal to 0 at axial location of 5-7 D_h downstream of spacer, then increasing, it reaches at its steady value of 0.03m^2/s^2. Case-5 has all mentioned characteristics with a higher entrance value as well as case-2.

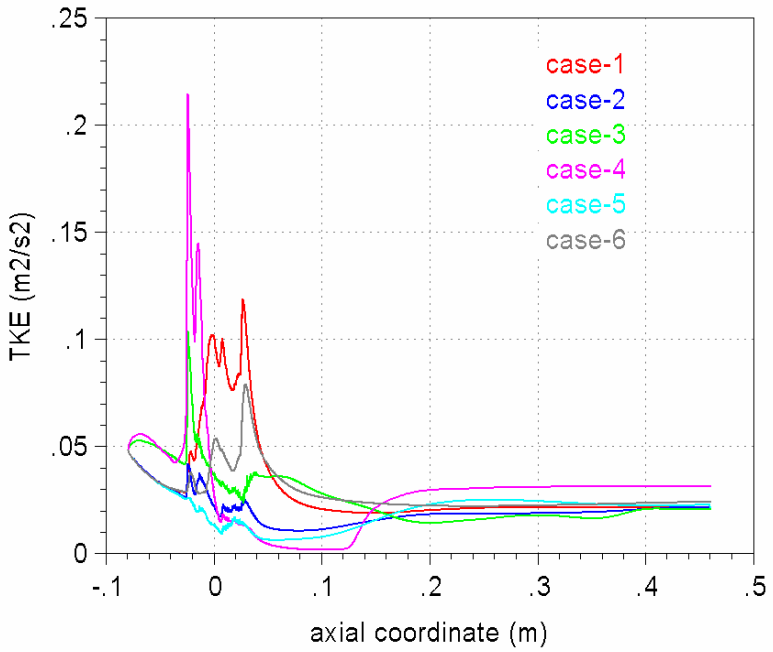

Figure 4.6 Axial variation of TKE over central line: grid spacer.

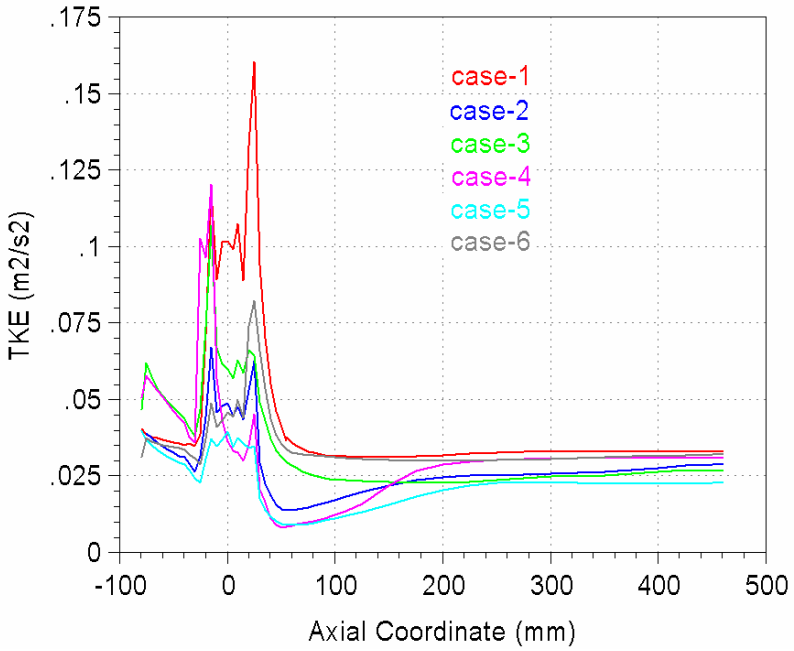

Figure 4.7 Axial variation of averaged TKE: grid spacer.

4.2.2. Ferrule Spacer

The inlet boundary conditions for ferrule spacer are prepared in the same way as in the case of grid spacer except of developing region lengths. In order to obtain inlet profiles for the ferrule spacer runs, 160mm-developing region for case-6 and 7, and 335mm-developing region for the others were prepared. Velocity magnitude and turbulent kinetic energy curves were obtained averaged in x-y planes axially and over a central line from inlet to exit of the subchannel. The velocity and TKE plots averaged axially and over a central line are given in Figures 4.8 to Figure 4.11. Also velocity magnitude contour plots at the end of the spacer region, z=14mm, for case-7 and case-10 in Figure 4.12, and an additional contour plot with axial and lateral velocity magnitude profiles with a different view in Figure 4.13 are given.

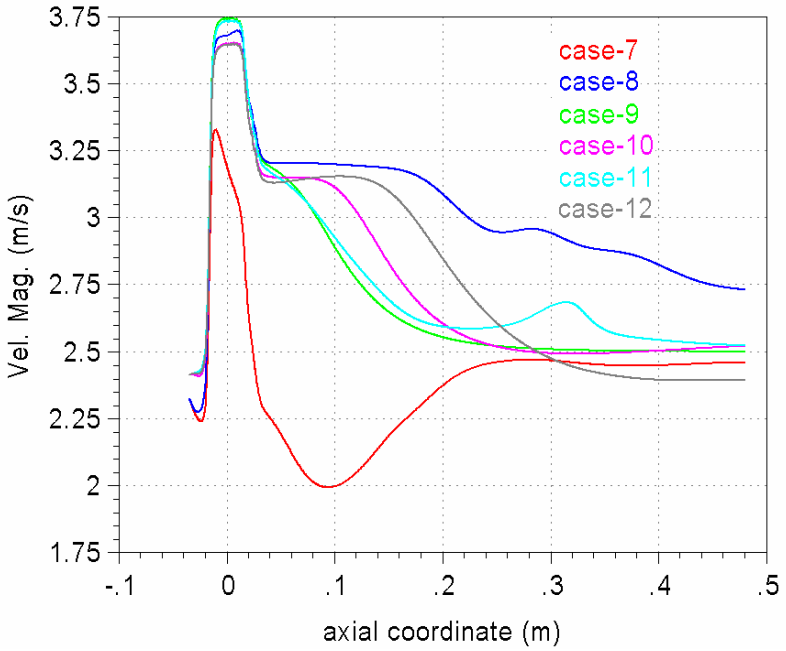

Figure 4.8 Axial variation of velocity magnitude over central line: ferrule spacer.

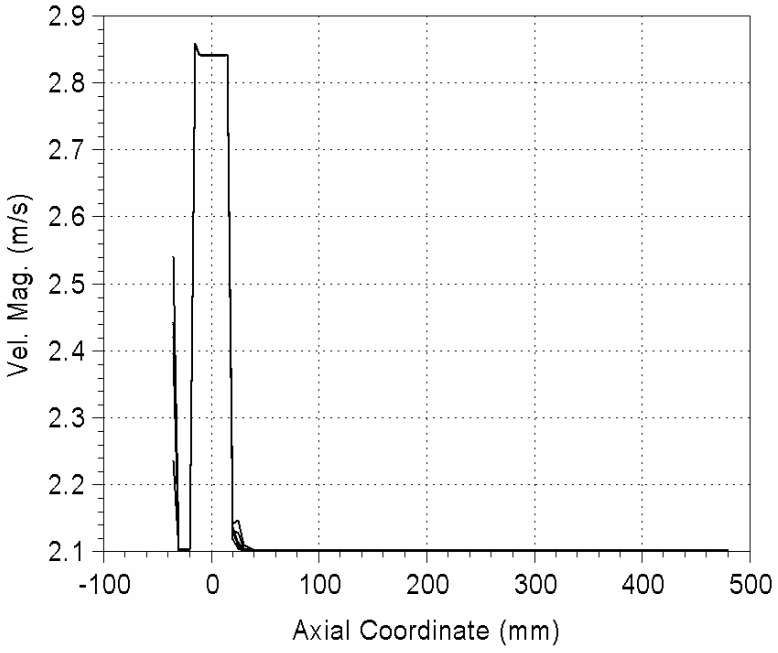

Figure 4.9. Axial variation of averaged velocity magnitude: ferrule spacer.

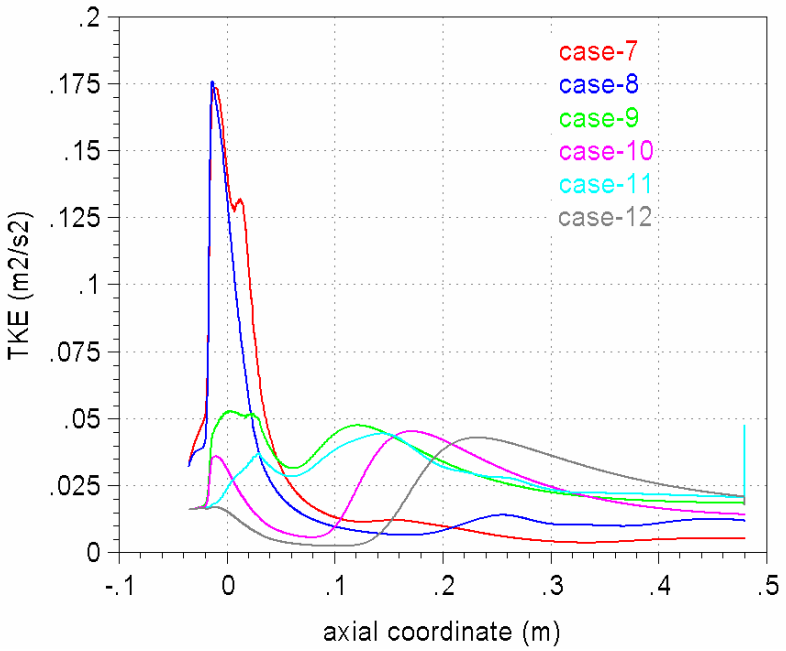

Figure 4.10 Axial variation of TKE over central line: ferrule spacer.

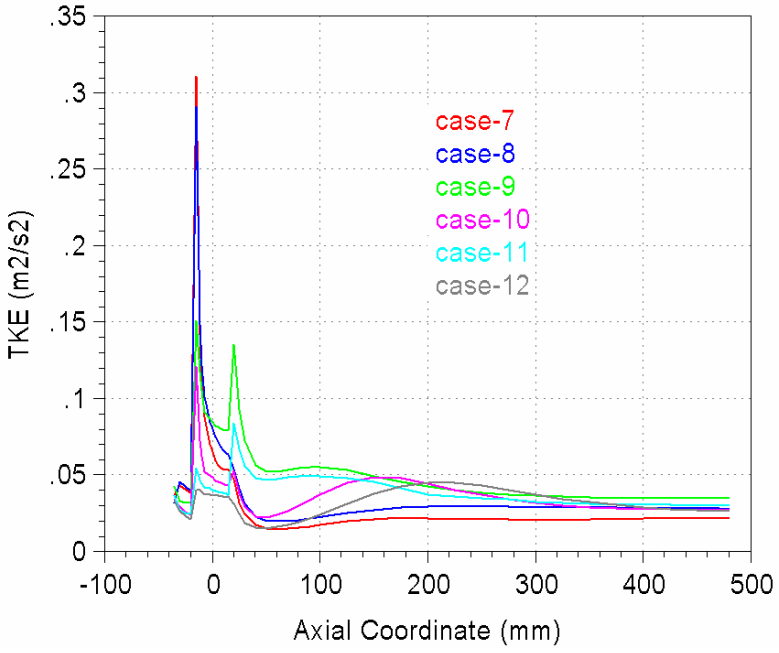

Figure 4.11 Axial variation of averaged TKE: ferrule spacer.

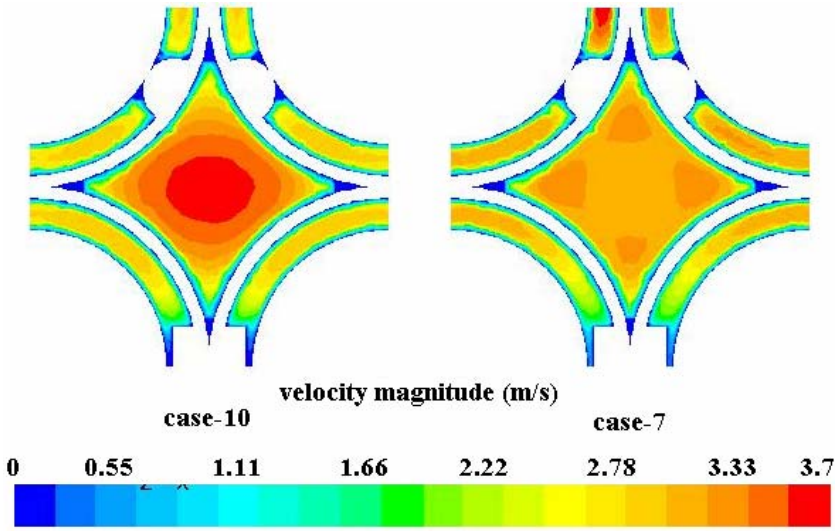

Figure 4.12. Velocity Magnitude Contour Plots at z=14mm.

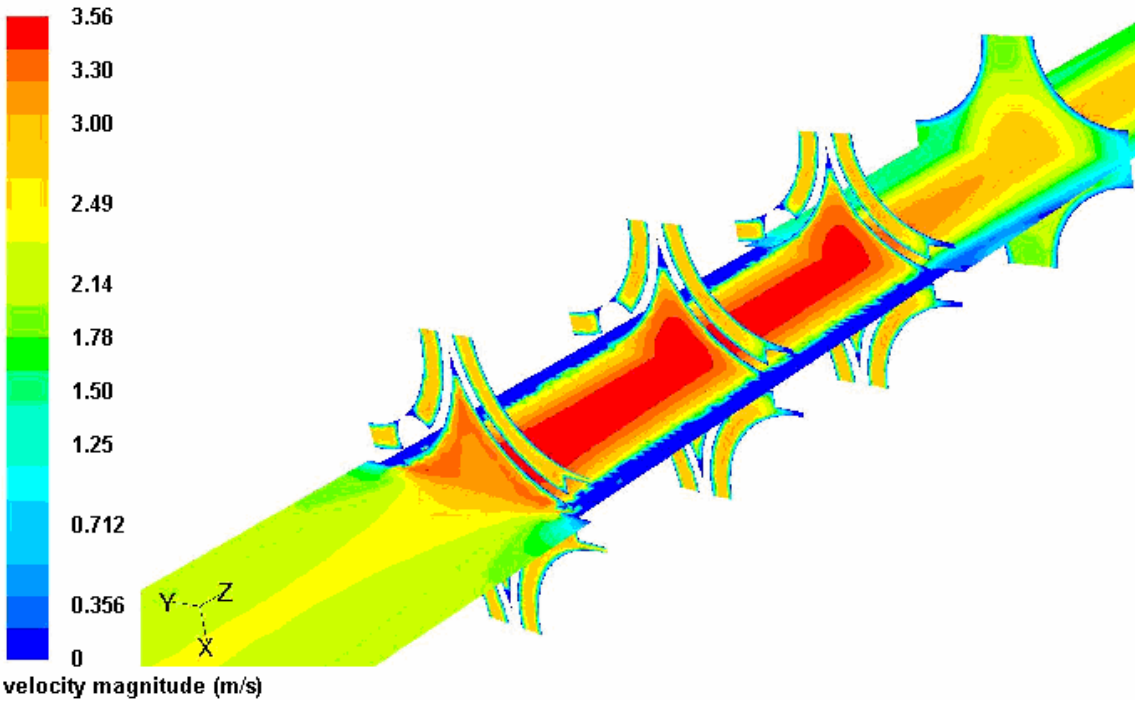

Figure 4.13 A view of velocity magnitude contour for ferrule spacer.

As seen from the velocity magnitude curves, the maximum velocity is reached at in the middle of the spacer after a sharp increase at spacer inlet. Case-7 has its maximum velocity magnitude value of 3.3 m/s, while others of 3.7, 3.8 m/s. In-spacer velocity magnitude shapes of all cases for ferrule type are very similar to each other.

After exiting the spacer region, they have small differences. Cases 8, 10 and 12 have constant value up to 8 D_h downstream of spacer and decrease to their steady value of 2.6 m/s at axial location of about 32 D_h, very close to exit of subchannel. While cases 9 and 11 tends to decrease directly to their fully developed value of 2.6 m/s, at axial locations of 20 and 32 Dh downstream of spacer, respectively. Case-7 has a different behavior from others, that is, after exiting the spacer velocity magnitude curve decreases to its minimum value of 2 m/s at axial location of 5 D_h, and then increases to its relatively constant value of 2.5 m/s at axial location of 16 D_h.

Turbulent kinetic energy curves, in a rude way, splits into two types. One of which is consisted of case-7 and case-8, as being the k-ω models with standard and enhanced wall treatment, respectively. These curves had a peak maximum value at the center of the spacer and strictly decrease to their relative constant values at axial location of 5 D_h. However, the other type, as seen in cases 9, 10, 11, and 12, had two local maximum points one of which is reached at the center of the spacer in all cases, and other at different axial locations of 7.5, 11, 10, and 15 D_h downstream of spacer, respectively. In order to explain this behavior velocity magnitude contours just before the exit of spacer region, that is at axial point of z = 14mm, for which have different TKE behaviors of case-10 and case-7 are given in Figure 4.12. Fluid is separated as central and outer regions by the spacer walls. In case-7, average velocity magnitude in outer region and central region is close to each other, while the difference is relatively great in case-10. Fluid with different velocity magnitude values mixes after exiting the spacer region and causes a turbulent kinetic energy increase.

4.3. Pressure Drop

Pressure drop across the spacer region for both grid and ferrule type spacer was calculated. A 110mm-distance spacer region (7.4 D_h) in axial direction, as in the BFBT specifications, was specified for pressure drop calculations. Table 4.1 presents pressure drop results obtained at Reynolds Number of 240000. For grid type spacer, pressure drop values vary between 3.00 to 4.10 kPa. An additional bare rod subchannel configuration without spacer was prepared with the same length

(110mm), in order to understand spacer effect on pressure drop. The resulting pressure drop is 0.35 kPa. For ferrule type spacer, values range from 2.58 to 3.60 kPa. Sample pressure plots across subchannel of grid and ferrule types are given with bare rod plots in Figure 4.14. Bundle-averaged pressure drop value over ferrule spacer was declared as 2.06 kPa, in the BFBT benchmark. The experimental bundle-averaged value is largely overestimated as compared to results with subchannel approach in the present study.

Table 4.1 Pressure drop results.

case#	spacer-type	turb. model	wall treatment	pressure drop (kPa)
case-1	grid	k-ε Standard	enhanced	3.98
case-2	grid	k-ε Standard	standard	3.11
case-3	grid	k-ω Standard	enhanced	3.20
case-4	grid	k-ω Standard	standard	4.10
case-5	grid	RSM	standard	3.03
case-6	grid	RSM	enhanced	3.69
case-7	ferrule	k-ω Standard	standard	3.59
case-8	ferrule	k-ω Standard	enhanced	3.34
case-9	ferrule	k-ε Standard	enhanced	3.28
case-10	ferrule	k-ε Standard	standard	2.65
case-11	ferrule	RSM	enhanced	3.07
case-12	ferrule	RSM	standard	2.58

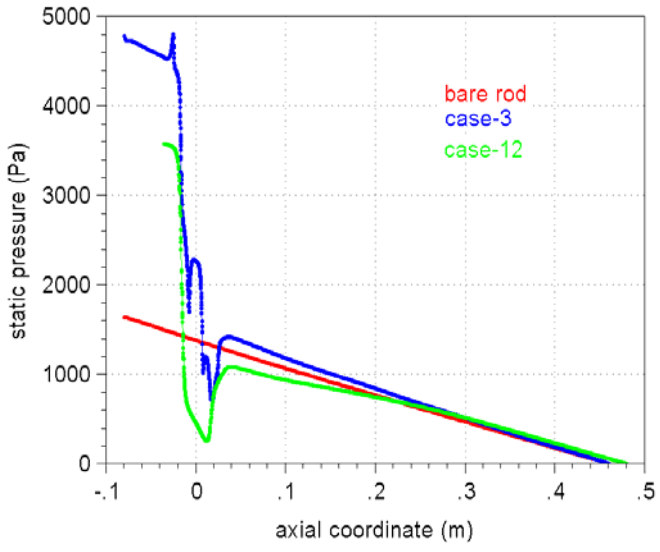

Figure 4.14. Static pressure plot along subchannel.

4.4. Heat Transfer

Enhancement of heat transfer in subchannels is one of most important subjects in thermal-hydraulics of nuclear reactors. Spacer grids provide an effective method to enhance turbulent heat transfer by mixing the flow in subchannels.

Heat transfer calculations were made for each type of the spacers by applying a constant temperature to the inlet of the fluid, and a constant heat flux to fuel walls across the subchannel with the cases studied in the fluid dynamics section. Water was the working fluid with a Reynolds Number of 240000. Inlet temperature of 557K was applied to water at inlet and 200 kW/m^2 of constant heat flux from fuel surface.

4.4.1. Heat Transfer Enhancement: grid spacer

A Nusselt Number study was performed by taking averages over fuel surface in spacer region, that is between ±24.35mm in axial direction, for all cases with an additional bulk subchannel case. The results are given in Table 4.2. with percent Nusselt Number enhancements compared to bare rod subchannel case . As can be seen from the results, on the average, 4% area averaged Nusselt Number enhancement provided by the grid type spacer. Case-2 and case-5, which are k-ε and RSM models with standard wall treatment, gave relatively smaller results compared to others.

Table 4.2 Average Nusselt number values and percent increase.

case#	Nu Avg.	% increase
1	1181.9	5.1
2	1152.7	2.7
3	1177.1	4.7
4	1179.2	4.9
5	1149.5	2.4
6	1173.2	4.4

case-#	Nu Avg.	% increase
7	1178.4	4.4
8	1177.2	4.3
9	1178.5	4.4
10	1158.4	2.7
11	1171.5	3.8
12	1156.2	2.5

In order to understand the heat transfer characteristics better, circumferentially averaged axial (CAA) values of Nusselt Number along subchannel are plotted. The cross plot of CAA Nusselt Number for grid spacer cases is given in figure 4.15. In spacer region, values are greater than the ones in bare rod up to a value of 70, then this difference decreases up to 30 downstream of spacer. The curves decrease through spacer at the beginning and then increase step by step at each spacer area change, having a maximum value at the center. Axial decay of the CAA Nusselt number is very rapid just after the spacer region and tends to decrease slowly through the bare rod region. An increase in the values of case-4 can be seen after the spacer region. This effect can also be seen from the velocity magnitude plots over a central line along subchannel, as mentioned in axial velocity magnitude variation item, section 4.2.

Nusselt Number hand-calculations has also been made by using Dittus-Boelter correlation for mean fluid velocity magnitude of 2.1 m/s for inlet and 2.53 m/s at the center of the spacer, for the constant fluid properties documented, resulting values of 1000 and 1106, respectively. The difference between calculated Nusselt Number and CFD result did not exceeded a value of 12% in extreme cases.

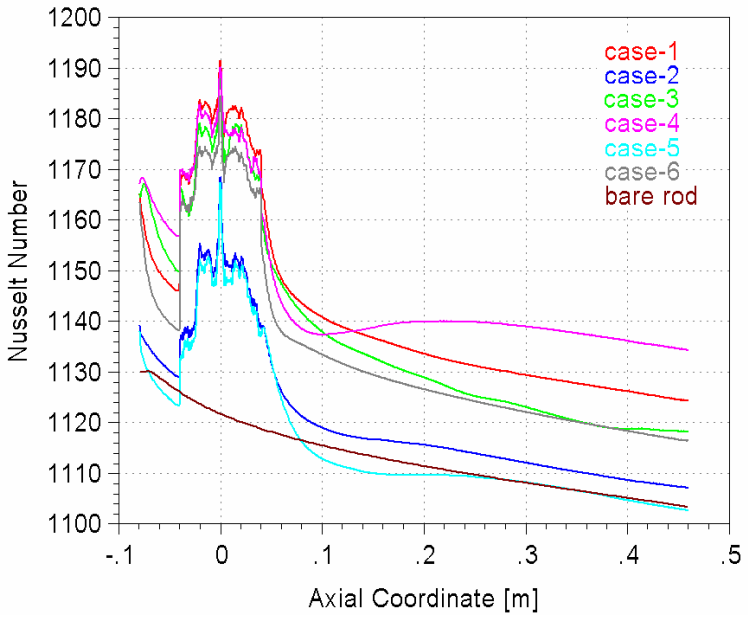

Figure 4.15 CAA Nusselt number along fuel rod surface: grid spacer.

4.4.2. Temperature Distribution on Fuel Surface

In nuclear reactor technologies, fuel surface temperature is a critical design parameter. The integrity of the fuel rods can be compromised if the local temperatures on the surface of the rods are too large. Larger and more uniform single-phase, local heat transfer coefficients yield increased performance, and prevent potential damage to the fuel rods those would result from areas of increased temperature.

In the cases studied for grid spacer, fuel surface temperature distribution, hot spot values and regions formed, and axial variation of average circumferential temperature values are documented. Contours of temperature for the grid spacer cases and additional bare rod case, from -40mm to 160mm, approximately 10 D_h, along fuel surfaces are given in figure 4.16. The spacer center is located at z=0 mm in axial direction. Figures are scaled by a factor of 3 in axial direction for easy comparison and for better visualization. Coloration of contours, that corresponds to fuel surface temperature values, were determined by pre-identifying the minimum and maximum values, between 560 and 595K, over the region examined and fixed for all grid spacer cases.

As seen from the figure for bare rod subchannel, fuel surface temperature increases uniformly along axial direction. For other cases, fuel surface temperature is significantly decreased in the spacer region. The difference between spacer region and bare rod subchannel fuel surface temperature reaches at up to 15K. At the center of the spacer, the closest point between fuel and spacer, a local cold region and after some distance just after this point, a local hot region is formed in all cases. The temperature values at the hot regions are between 578.4 K for case-4 and 592.5 K for case-5, which are around the temperature value in bare rod subchannel case. The maximum cooling of the fuel surface temperature in spacer region is obtained in cases-1 and 4. The minimum cooling effect of spacer can be seen in case-2 and case-5, which was obvious in Nusselt Number behaviors. Also for these cases, a hot spot region is formed after spacer region extending into axial direction and tending to

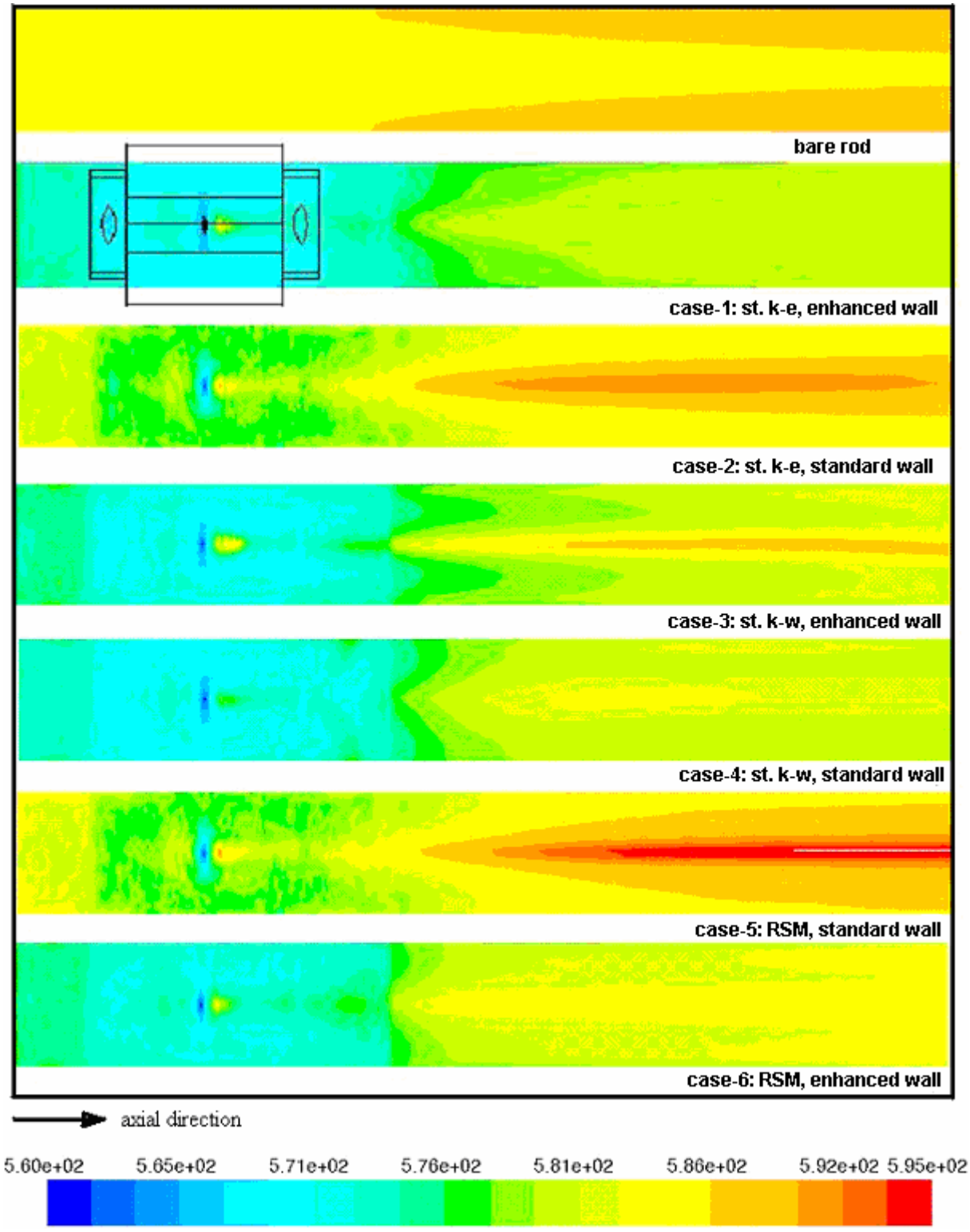

Figure 4.16. Contours of fuel surface temperature: grid spacer, coloration T (K).

disappear after some distance. Furthermore, the hot spotted values exceed the values in the bare rod subchannel case. For cases-1, 3, 4, and 6, axial increase of fuel surface temperature is more uniform.

Circumferentially averaged axial fuel surface temperature distribution is plotted for all cases including bare rod subchannel case in figure 4.17. Enhancement in heat transfer along spacer region caused a significant decrease in circumferentially averaged fuel surface temperature. A maximum of 17K-difference at the center of the spacer, and 8K-difference at the exit of the subchannel is obtained in some cases. However, after-spacer profiles of case-2 and especially case-5 are nearly the same as the profile in bare rod subchannel case.

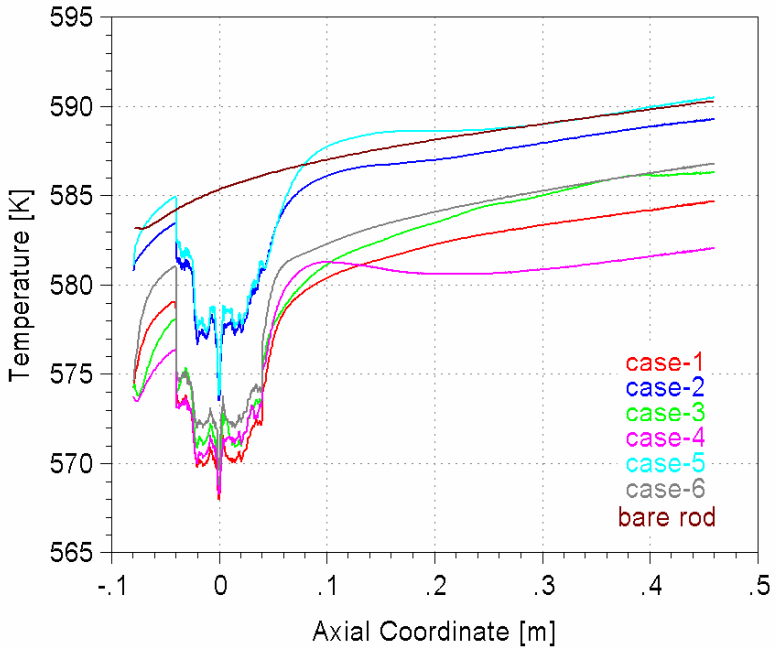

Figure 4.17 CAA fuel rod surface temperature: grid spacer.

4.4.3. Heat Transfer Enhancement: ferrule spacer

The ferrule type spacer is located at the center of the coordinate axes and extends from -15.5mm to 15.5mm in axial direction. Area averaged Nusselt number values on the fuel surface corresponding to spacer location are calculated. The results are given in table 4.2 with percent Nusselt Number enhancements compared to bare rod

subchannel case. On the average, 3.7% area averaged Nusselt number enhancement provided by the ferrule type spacer. Cases 10 and 12, which are k-ε and RSM models with standard wall treatment, as in the case of grid spacer, gave relatively smaller results compared to others. This significant difference can said to be originated from the wall treatment of the model and the near-wall mesh density pair.

Circumferentially averaged axial values of Nusselt Number for all cases including bare rod subchannel case was plotted. The cross plot is given in figure 4.18. The values ranged between 1100 and 1190. CAA Nusselt Number values sharply increases at the inlet of the spacer because of the abrupt flow area change. A maximum 5.3% of circumferentially averaged heat transfer enhancement in the spacer region is obtained at this point. After entering into the spacer, since there is no flow area change until exit, Nusselt values decrease and drop sharply at exit.

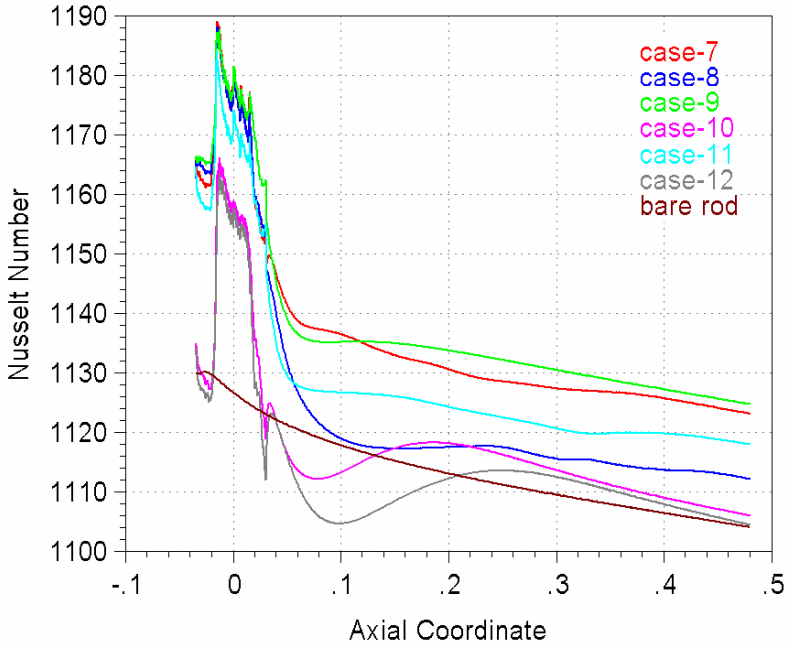

Figure 4.18. CAA Nusselt number over fuel rod surface: ferrule spacer.

4.4.4. Temperature Distribution on Fuel Surface

Fuel surface temperature contours including bulk subchannel (at the top of figure 4.17) case between axial location of -35 to 30mm are given in figure 4.19. Only a

quarter of the bulk subchannel fuel surface is given while others are from one symmetric side of a full subchannel. Temperature values range between 562 and 674K. This difference may be attributed to the values between very narrow zones at the corners and at open flow areas. A cold temperature region is formed at the lower part of spacer inlet and a hot temperature region at the upper part around the intersection of fuel surface and spacer, in all cases. Cold region temperature is 562K, nearly the same in all cases, and hot region ranges between 596K in case-10 and 674K in case-8. For an overall understanding of the fuel surface temperature variation, CAA values are plotted in figure 4.20. 15K of maximum CAA temperature drop can be seen at the inlet of the ferrule spacer.

4.5. Fluid Temperature Distribution Downstream of Spacer

Temperature contours, ΔT, at just exit of the spacers and at downstream of 5 D_h are given in figure 4.21, and figure 4.22, respectively for grid and ferrule type spacers. ΔT is defined by the scale of static temperature value at the point interested minus temperature value at the inlet boundary condition of 557 K, as reference point.

For grid type spacer, only results of case-1 and case-3 are considered while for the ferrule type they are of case-7 and case-9. Grid spacer extends from -24.35 mm to 24.35 mm in axial direction, and contours at the exit are captured at z = 25 mm. As can be seen from these very near-region contours, a 16-K temperature difference can be observed, from center of the subchannel to fuel surface. As getting further into the subchannel through $5D_h$ downstream of spacer, non-uniformity increases, and ΔT reaches at a value of 30 K. This effect can be explained by the axial development of velocity magnitude plots, for case-3, which has a local minimum around 5 D_h.

At the exit of the ferrule type spacer, ΔT reaches at a value of 35K because of the stagnation region located at the bottom of subchannel, on the page-plane, where velocity of the fluid relatively smaller compared to values in central region. As the flow progresses into the subchannel through $5D_h$, spacer effect disappears and a relatively uniform temperature profile is developed with ΔT of 30K.

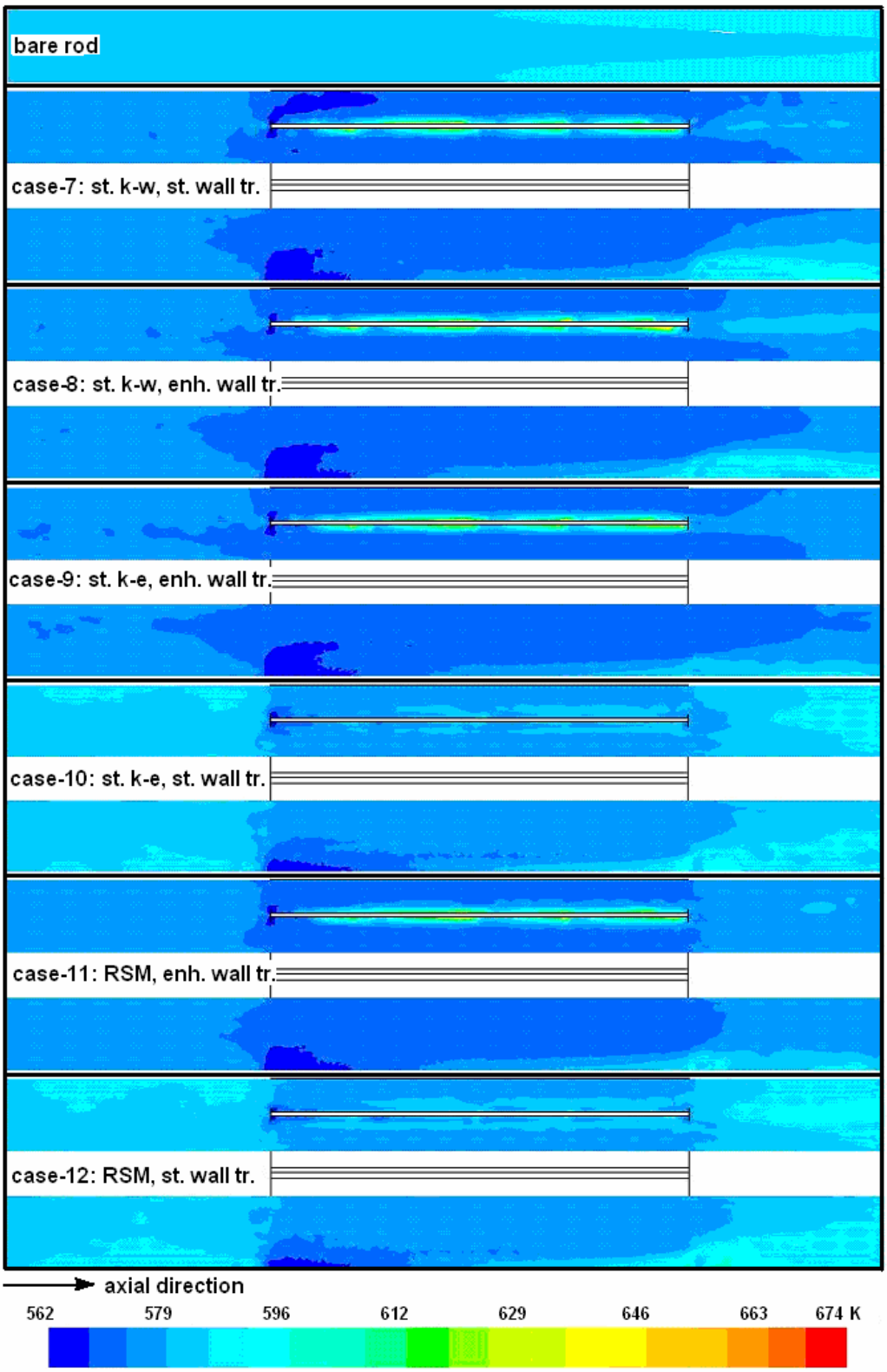

Figure 4.19 Fuel surface temperature contour plots: ferrule spacer.

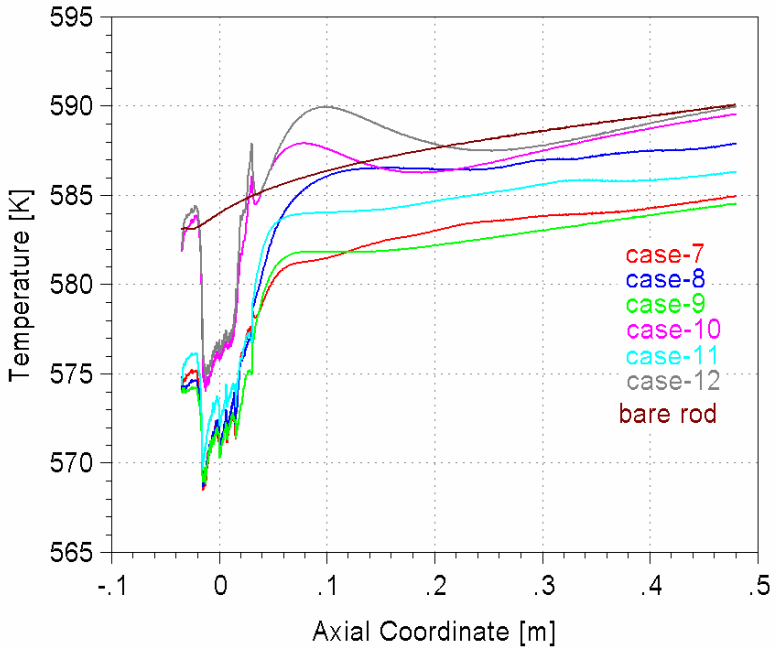

Figure 4.20 CAA fuel surface temperature: ferrule spacer.

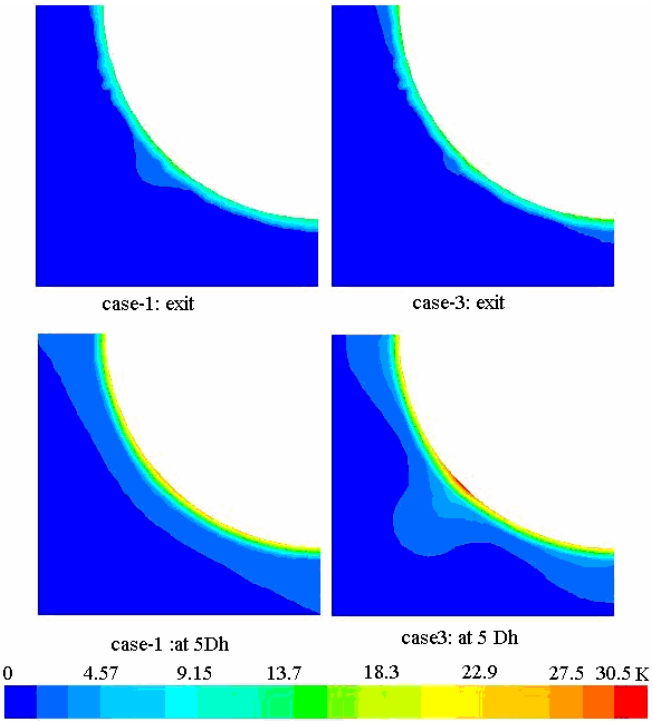

Figure 4.21 Temperature difference contours: grid spacer.

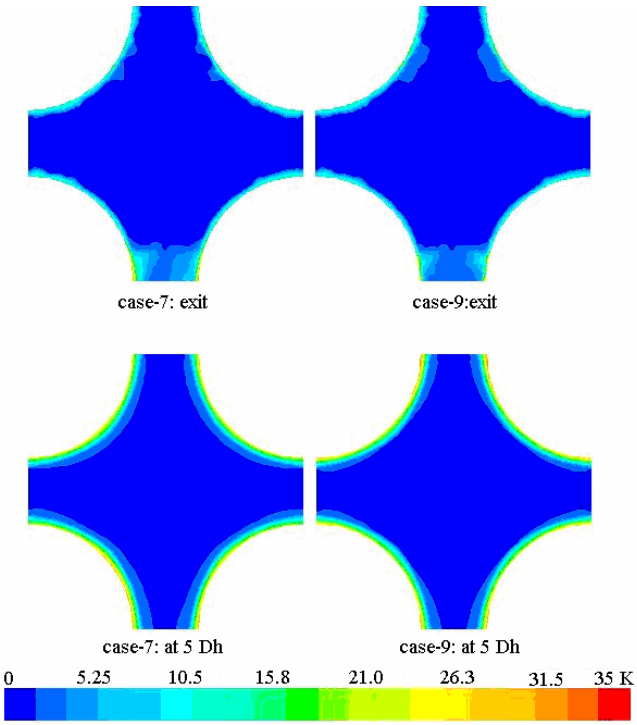

Figure 4.22 Temperature difference contours: ferrule spacer.

5. MODELING SPACER

In the first part of the present study, spacer effects on flow dynamics and heat transfer in subchannels, representative of infinite fuel bundle, was investigated. The results for the two spacer types are documented and compared to available experimental data. In this part, an alternative method to model the spacer behavior is studied.

Construction of a detailed computational domain, meshing its complex geometry, and run-time difficulties may be overcome by application of external user-defined source terms and porous media approaches to particular nuclear reactor in-core CFD investigations. The porous media model can be used for a wide variety of problems, including flows through packed beds, filter papers, perforated plates, flow distributors, and tube banks. Moreover, addition of external source terms to the standard fluid flow equations allows customizing the existing models for special needs. The porous media model incorporates an empirically determined flow resistance in a region of the

model defined as porous. In essence, the porous media model is nothing more than an added momentum sink in the governing momentum equations [FLUENT ug, 2006].

5.1. Source Term Definitions

Porous media are modeled by the addition of a momentum source term to the standard fluid flow equations. The source term is composed of two parts: a viscous loss term, and an inertial loss term.

$$S_i = -\left(\sum_{j=1}^{3} D_{ij} \mu v_j + \sum_{j=1}^{3} C_{ij} \frac{1}{2} \rho v_{mag} v_j \right) \tag{5.1}$$

where S_i is the source term for the ith (x, y, or z) momentum equation, and D and C are prescribed matrices. This momentum sink contributes to the pressure gradient in the porous cell, creating a pressure drop that is proportional to the fluid velocity (or velocity squared) in the cell.

The first term, viscous loss term, in Equation 5.1 is ignored in this case. At high flow velocities, the constant C in Equation 5.1 provides a correction for inertial losses in the porous medium. This constant can be viewed as a loss coefficient per unit length along the flow direction, thereby allowing the pressure drop to be specified as a function of dynamic head. In order to capture the pressure behavior, pressure drop obtained from the first part, for case-1, was used to determine the constant C in Equation 5.1. The porosity in the spacer region was calculated dividing the fluid volume by spacer volume, which is 0.872.

An external turbulent kinetic energy source term was defined to represent spacer given by,

$$S_{TKE} = \frac{k_{sp}}{L_{sp}} \frac{\rho}{2} |v|^3 \tag{5.2}$$

where k_{sp} is pressure loss coefficient, L_{sp} is the length of spacer in axial direction, ρ is the fluid density, and v is velocity at the computation point. This TKE source results a dissipation rate (TDR) source term of the form given by

$$S_{TDR} = C_{1\varepsilon}\frac{\varepsilon}{k}S_{TKE} \tag{5.3}$$

where $C_{1\varepsilon}$ is one of the model constants of k-ε model, defined in Table 2.1.

5.2. Solution

The bare rod subchannel geometry was constructed, as in the case of grid spacer, and meshed using GAMBIT software. The mesh was coarse as compared to ones in the first part. The bulk spacer region located at the center of the axial coordinate was identified for porous media. The porous media parameters defined in the previous section were calculated using the results of case-1 in the first part, and applied to porous spacer region. The TKE and TDR source terms are coded by C programming language as a FLUENT user-defined function (UDF is given in Appendix-D). This function, valid only for the spacer region, was attached to the fluid. The same boundary conditions of wall, heat flux, fully developed inlet profile and inlet temperature, were applied. The standard k-ε model was employed for the solution and results were obtained.

5.3. Results and Comparison

Reasonable results were obtained in pressure, turbulent kinetic energy, and its dissipation rate by using porous media approach for momentum source, user-defined source terms for TKE and TDR. However, the velocity behavior in the spacer region was not captured well, since there is no physical spacer body in porous media. The cross plots with the results of case-1 for pressure, velocity magnitude, TKE, and TDR along with the same line are given in Figure 5.1, Figure 5.2, Figure 5.3, and Figure 5.4, respectively.

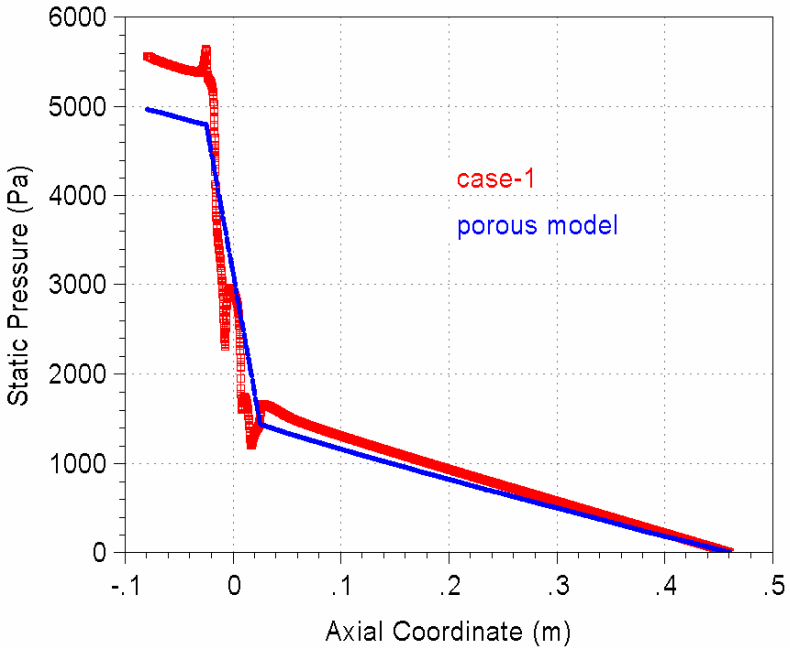

Figure 5.1. Axial static pressure variation along subchannel

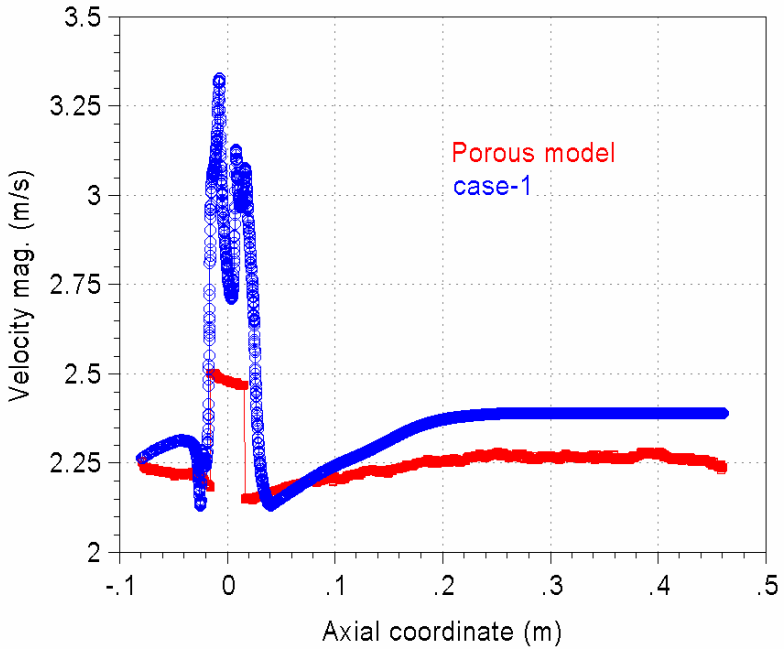

Figure 5.2. Axial Velocity variation along subchannel.

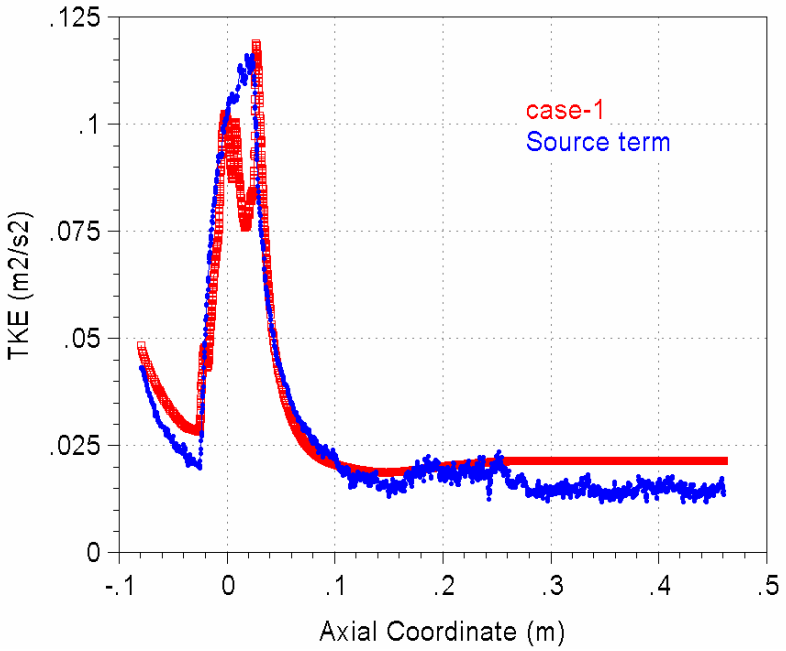

Figure 5.3. Axial TKE variation along subchannel.

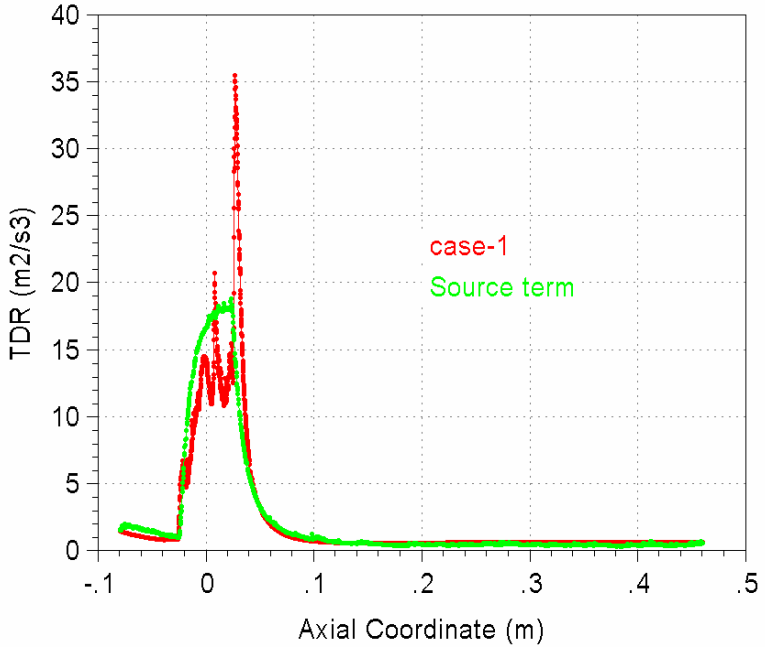

Figure 5.4. Axial TDR variation along subchannel.

As presented in Figure 5.1, pressure curve of porous media model is quite close to result of case-1. TKE and TDR results from Figure 5.3, and 5.4 are also consistent. In the results of source term model for the spacer, the TKE curve uniformly increases converging to the maximum point, reached at the end of spacer region, while in case-1, some sharp variations take place. The same situation is also valid for TDR curve. These fluctuations are due to the walls of spacer that exist physically in the subchannel. But if averages of TKE or TDR over lateral planes along axial direction were taken, more smooth curves like source term model could have been obtained. Out of in-spacer region behavior, axial decay of the turbulent variables is also in good agreement. However, the same consistency obtained in these variables was not obtained in velocity variations. Velocity magnitude in case-1 increases fluctuating in the spacer region as the result of the irregular area contraction due to spacer, while it is smoother in the source term model since no physical body exists.

6. CONCLUSIONS AND RECOMMENDATIONS

Effects of spacers, used in the LWR fuel bundles, on turbulent flow and heat transfer characteristics were examined in the study by using subchannel approach. The geometry specifications and operational conditions for single-phase cases declared in BFBT [OECD/NRC Benchmark,2004] were used in the setup of the CFD study. Grid and ferrule type spacers were investigated with the same fuel rod diameter and pitch by using commercially available CFD software FLUENT. The flow across the fuel bundle with a Reynolds number of 240000 corresponding to one of the single-phase cases in BFBT, was simulated with different turbulence models. The pressure drop, axial variation of lateral flows and turbulence behavior, heat transfer, temperature distribution of fuel walls and coolant over the subchannel was documented.

The performance of turbulence models and spacer designs used in the simulation were compared to each other. Strong lateral velocity fields up to 30% of axial flow and swirling structures developed in grid spacer region, while almost no lateral structures seen in ferrule type. The turbulence models of k-ε and RSM with standard wall treatment gave closer pressure drop results over spacer region to the declared bundle averaged values of BFBT experiment with respect to k-ω model. However, as

with the wall y^+ values of the present study, near-wall solutions of cases with standard wall treatment were failed. On the average, pressure drop values of 3.53kPa and 3.1kPa for grid and ferrule type, respectively, were obtained from the CFD results. Altough averaged Nusselt number results obtained from the CFD analysis with enhanced wall treatment are quite close to each other, when compared to one calculated with Dittus-Boelter correlation, k-ω (case-3) for grid and RSM (case-12) for ferrule spacer are the most consistent models. Analysis showed a 8% greater heat transfer enhancement in grid spacer region than the ferrule spacer, but the turbulence tends to increase downstream of spacer for most cases in ferrule type (Figure 4.10.), resulting a relative enhancement in heat transfer, while no significant heat transfer increase seen in downstream region of grid spacer. Quite consistent of TKE, TDR, and pressure drop results were obtained from the second part, Spacer Modeling section. However, other variables such as velocity components did not show that consistency. Considerable savings in mesh generation and computational time can be obtained with porous media approach.

Very detailed geometries of the two types of spacer were modeled, and meshed, practical, and standard versions of the two equation turbulence models were employed for the solutions. Different mesh configurations, better or coarser, for more consistent results, mesh dependency and different operational conditions for deeper understanding of the solution should have been investigated. A subchannel approach was used in the present investigation, but, in order to obtain closer results to experimental data, fuel bundle approach must be studied. From the source term modeling of spacer study, it is clear that detailed investigations may give challenging results.

REFERENCES

Aszódi, A., Légrádi, G.: Detailed CFD analysis of coolant mixing in VVER-440 fuel assemblies with the code CFX-5.5. Technical Meeting on Use of Computational Fluid Dynamics (CFD) Codes for Safety Analysis of Reactor Systems, Including Containment. Pisa, Italy, 11-14 November 2002. (from announced "Evaluation of CFD methods for reactor safety analysis", 1998-2002, European Commission 5th Euratom Framework Programme.)

Conner, M. E., Smith, L. D.: Study of flow distribution and heat transfer in PWR fuel. Trans. ANS 86 (2002), 152 – 153.

Creer, J. M., Rowe, D. S., Bates, J. M., Sutey, A. M.: Effects of sleeve blockages on axial velocity and intensity of turbulence in an unheated 7 x 7 rod bundle. BNWL-1965, January 1976, Battelle Pacific Northwest Labs.

Gango, P.: Application of CFD models for 3D analysis of single-phase thermal-hydraulics in the VVER-440 fuel assembly, abstracted from announced "Evaluation of CFD methods for reactor safety analysis", 1998-2002, European Commission 5th Euratom Framework Programme.

Hinze JO. Turbulence. McGraw-Hill Publishing Co., 1975, New York.

FLUENT user guide, 2006, FLUENT INC.

Karoutas, Z., Gu, C. Y., Scholin, B.: 3-D flow analyses for design of nuclear fuel spacers, 1995, abstracted from announced "Evaluation of CFD methods for reactor safety analysis", 1998-2002, European Commission 5th Euratom Framework Programme.

OECD/NRC Benchmark based on NUPEC BWR Full-size Fine-mesh Bundle Tests (BFBT), Assembly Specifications and Benchmark Database, October 4, 2004, Incorporated Administrative Agency, Japan Nuclear Energy Safety Organization, JNES-04N-0015.

Tzanos, C. P.: Performance of k – ε turbulence models in the simulation of LWR fuel bundle flows. Trans. ANS 84 (2001), 197 – 199.

Tzanos, C. P.: Large Eddy Simulation of flow in LWR fuel bundles. Trans. ANS 85 (2001a), 261 – 262.

Tzanos, C. P.: Performance of the RNG and two-layer k – ε models in the simulation of LWR fuel-bundle flows. Trans. ANS 86 (2002), 148 – 150.

Weber, D. P., Wei, Y. C., Rock, D. T., Rizwan-Uddin, Brewster, R., Jonnavithula, S.: Computational Fluid Dynamics (CFD) and its potential for nuclear applications. Proc. American Power Conference, Vol. 61-I, 338-348, Chicago, USA, 1999.

Weber, D. P., Wei, T. Y. C., Brewster, R. A., Rock, D. T., Rizwan-Uddin: High fidelity thermal-hydraulic analysis using CFD and massively parallel computers, 2001.

Yang, S. K., Chung, M. K.: Spacer grid effects on turbulent flow in rod bundle, 1998, Journals of Fluid Engineering, 120, pp. 786-791.

APPENDIX-A

Turbulence Models

A.1.1. k–ε Model

k-ε is one of the two-equation models in which the turbulent velocity and length scales are determined independently. Robustness, economy, and reasonable accuracy for a wide range of turbulent flows explain its popularity in industrial flow and heat transfer simulations.

The standard k-ε is a semi-empirical turbulence model based on transported variables, turbulence kinetic energy (k) and its dissipation rate (ε). Assuming the flow is fully turbulent, and the effects of turbulent viscosity is negligible, the equation for turbulence kinetic energy is derived from exact equation, while for its dissipation rate equation was obtained using physical reasoning. Transport equations for standard k-ε model are given as,

$$\frac{\partial}{\partial t}(\rho k)+\frac{\partial}{\partial x_i}(\rho k u_i)= \frac{\partial}{\partial x_j}\left[\left(\mu+\frac{\mu_t}{\sigma_k}\right)\frac{\partial k}{\partial x_j}\right]+G_k+G_b-\rho\varepsilon-Y_M+S_k \tag{A.1}$$

$$\frac{\partial}{\partial t}(\rho \varepsilon)+\frac{\partial}{\partial x_i}(\rho \varepsilon u_i)= \frac{\partial}{\partial x_j}\left[\left(\mu+\frac{\mu_t}{\sigma_\varepsilon}\right)\frac{\partial \varepsilon}{\partial x_j}\right]+C_{1\varepsilon}\frac{\varepsilon}{k}(G_k+C_{3\varepsilon}G_b)-C_{2\varepsilon}\rho\frac{\varepsilon^2}{k}+S_\varepsilon \tag{A.2}$$

μ_t is turbulent (or eddy) viscosity, and computed by combining k and ε as follows:

$$\mu_t=\rho C_\mu\frac{k^2}{\varepsilon} \tag{A.3}$$

The term G_k represents the production of turbulence kinetic energy, and can be modeled for the standard, RNG, and realizable k-ε models. From the exact equation for the transport of k, this term is defined as

$$G_k = -\rho\overline{u_i' u_j'}\frac{\partial u_j}{\partial x_i} \quad \text{(A.4)}$$

Or with the Boussinesq's approach

$$G_k = \mu_t S^2 \quad \text{(A.5)}$$

Where S is modulus of the mean rate-of-strain tensor, and defined as

$$S \equiv \sqrt{2S_{ij}2S_{ij}} \quad \text{(A.6)}$$

The term G_b represents the generation of turbulence due to buoyancy, and is given by

$$G_b = \beta g_i \frac{\mu_t}{Pr_t}\frac{\partial T}{\partial x_i} \quad \text{(A.7)}$$

where Pr_t equals to 0.85, and is the turbulent Prandtl number for energy and g_i is the component of the gravitational vector in the ith direction. The coefficient of thermal expansion, β, is defined as

$$\beta = -\frac{1}{\rho}\left(\frac{\partial \rho}{\partial T}\right) \quad \text{(A.8)}$$

The degree to which ε is affected by the buoyancy is determined by the constant $C_{3\varepsilon}$. In FLUENT, $C_{3\varepsilon}$ is not specified, but is instead calculated according to the following relation:

$$C_{3\varepsilon} = \tanh\left|\frac{v}{u}\right| \quad \text{(A.9)}$$

where v is the component of the flow velocity parallel to the gravitational vector and u is the component of the flow velocity perpendicular to the gravitational vector.

Y_M represents the contribution of the fluctuating dilatation in compressible turbulence to the overall dissipation rate. The model constants $C_{1\varepsilon}$, $C_{2\varepsilon}$, C_μ and σ_k, σ_ε, Prandtl

numbers for k and ε, respectively, are determined experimentally and their values are given in Table-A.1. S_k and S_ε are user-defined source terms.

Table A.1. Model constants of standard k-ε.

Constant	Value
$C_{1\varepsilon}$	1.44
$C_{2\varepsilon}$	1.92
C_μ	0.09
σ_k	1.0
σ_ε	1.3

All three k-ε models, standard, RNG, and realizable, have similar forms, with transport equations for k and ε, but differencing in the calculation of turbulent viscosity, the turbulent Prandtl numbers governing the turbulent diffusion of k and ε, and the generation and destruction terms in the ε equation.

The RNG k-ε model is derived from the instantaneous Navier-Stokes equations, using renormalization group (RNG) methods. This results small differences in model constants, terms and functions in the transport equations. Turbulent viscosity is obtained in such a way that low-Reynolds-Number and near-wall regions handled better and also FLUENT provides an option to account for the effects of swirl or rotation. The main difference between the RNG and standard k-ε models lies in the additional term in the ε equation which results the RNG is more responsive to the effects of rapid strain and streamline curvature than the standard k-ε model, which explains the superior performance of the RNG model for certain classes of flows.

In realizable k-ε model, additional to standard and RNG, FLUENT provides to satisfy certain mathematical constraints on the normal stresses, consistent with the physics of turbulent flows. The realizable k-ε model was also intended to address some deficiencies of other k-ε models by adopting a new eddy-viscosity formula involving a variable C_μ originally proposed by Reynolds, and a new model equation for dissipation (ε) based on the dynamic equation of the mean-square vorticity

fluctuation. This model has been extensively validated for a wide range of flows, including rotating homogeneous shear flows, free flows including jets and mixing layers, channel and boundary layer flows, and separated flows. For all these cases, the performance of the model has been found to be substantially better than that of the standard k-ε model.

A.1.2. Convective Heat Transfer Modeling in k-ε Models

Turbulent heat transfer is modeled by using the Reynold's analogy approach to turbulence momentum, and the energy equation is given by the following:

$$\frac{\partial}{\partial t}(\rho E) + \frac{\partial}{\partial x_i}\left[u_i(\rho E + p)\right] = \frac{\partial}{\partial x_j}\left(k_{eff}\frac{\partial T}{\partial x_j} + u_i(\tau_{ij})_{eff}\right) + S_h \quad \text{(A.10)}$$

where E is the total energy, k_{eff} is the effective thermal conductivity, and $(\tau_{ij})_{eff}$ is the deviatoric stress tensor, defined as

$$(\tau_{ij})_{eff} = \mu_{eff}\left(\frac{\partial u_j}{\partial x_i} + \frac{\partial u_i}{\partial x_j}\right) - \frac{2}{3}\mu_{eff}\frac{\partial u_i}{\partial x_i}\delta_{ij} \quad \text{(A.11)}$$

The term involving $(\tau_{ij})_{eff}$ represents the viscous heating, and is always computed in the coupled solvers. For the standard and realizable k-ε models, the effective thermal conductivity is given by

$$k_{eff} = k + \frac{c_p \mu_t}{Pr_t} \quad \text{(A.12)}$$

where k is the thermal conductivity and the default value of the turbulent Prandtl number is 0.85.

A.2. k-ω Model

Two types of k-ω model, the standard and shear stress transport (SST), present in FLUENT. One of the main differences of SST model from the standard one is the gradual change from the standard k-ω model in the inner region of the boundary

layer to a high-Reynolds-number version of the k-ε model in the outer part of the boundary layer, and the other lies in the formulation of modified turbulent viscosity to account for the transport effects of the principal turbulent shear stress. The standard k-ω model is an empirical model based on model transport equations for the turbulence kinetic energy (k) and the specific dissipation rate, that is ratio of ε to k [FLUENT ug, 2006].

A.2.1. Standard k-ω Model

The transport equations of the turbulent model variables k and ω, for the standard k-ω model used in this study, are as follows:

$$\frac{\partial}{\partial t}(\rho k) + \frac{\partial}{\partial x_i}(\rho k u_i) = \frac{\partial}{\partial x_j}\left(\Gamma_k \frac{\partial k}{\partial x_j}\right) + G_k - Y_k + S_k \tag{A.13}$$

and

$$\frac{\partial}{\partial t}(\rho \omega) + \frac{\partial}{\partial x_i}(\rho \omega u_i) = \frac{\partial}{\partial x_j}\left(\Gamma_\omega \frac{\partial \omega}{\partial x_j}\right) + G_\omega - Y_\omega + S_\omega \tag{A.14}$$

Where Γ_k and Γ_ω represent the effective diffusivity of k and ω, respectively, and calculated as follows:

$$\Gamma_k = \mu + \frac{\mu_t}{\sigma_k} \qquad \text{and} \qquad \Gamma_\omega = \mu + \frac{\mu_t}{\sigma_\omega} \tag{A.15}$$

where σ_k and σ_ω are the turbulent Prandtl numbers for k and ω, respectively. The turbulent viscosity, μ_t, is computed by combining k and ω as follows:

$$\mu_t = \alpha^* \frac{\rho k}{\omega} \tag{A.16}$$

A low-Reynolds-Number correction is carried out by coefficient α^* damping the turbulent viscosity, given as:

$$\alpha^* = \alpha_\infty^* \left(\frac{\alpha_0^* + Re_t / R_k}{1 + Re_t / R_k} \right) \tag{A.17}$$

where

$$Re_t = \frac{\rho k}{\mu \omega}, \quad R_k = 6, \quad \alpha_0^* = \beta_i / 3 \text{, and } \beta_i = 0.072 \tag{A.18}$$

G_k represents the generation of turbulence kinetic energy due to mean velocity gradients. From the exact equation for the transport of k, this term is defined as

$$G_k = -\rho \overline{u_i' u_j'} \frac{\partial u_j}{\partial x_i} \tag{A.19}$$

Or with the Boussinesq's approach

$$G_k = \mu_t S^2 \tag{A.20}$$

Where S is modulus of the mean rate-of-strain tensor, and defined as

$$S \equiv \sqrt{2 S_{ij} 2 S_{ij}} \tag{A.21}$$

G_ω represents the generation of ω and given by

$$G_\omega = \alpha \frac{\omega}{k} G_k \tag{A.22}$$

The coefficient α is given by

$$\alpha = \frac{\alpha_\infty}{\alpha^*} \left(\frac{\alpha_0 + Re_t / R_\omega}{1 + Re_t / R_\omega} \right) \tag{A.23}$$

where $R_\omega = 2.95$. α^* and Re_t are given by Equations A.17 and A.18 respectively.

Y_k and Y_ω represent the dissipation of k and ω due to turbulence.

$$Y_k = \rho\beta^* f_{\beta^*} k\omega \tag{A.24}$$

where

$$f_{\beta^*} = \begin{cases} 1 & \chi_k \le 0 \\ \dfrac{1+680\chi_k^2}{1+400\chi_k^2} & \chi_k > 0 \end{cases} \tag{A.25}$$

where

$$\chi_k = \frac{1}{\omega^3}\frac{\partial k}{\partial x_j}\frac{\partial \omega}{\partial x_j} \tag{A.26}$$

and

$$\beta^* = \beta_i^* \left[1 + \xi^* F(M_t)\right] \tag{A.27}$$

$$\beta_i^* = \beta_\infty^* \left(\frac{4/15 + \left(Re_t/R_\beta\right)}{1 + \left(Re_t/R_\beta\right)^4} \right) \tag{A.28}$$

$$\xi^* = 1.5 \tag{A.29}$$

$$R_\beta = 8 \tag{A.30}$$

$$\beta_\infty^* = 0.09 \tag{A.31}$$

where Re_t is given by Equation A.18.

Dissipation of ω is given by

$$Y_\omega = \rho\beta f_\beta \omega^2 \tag{A.32}$$

where

$$f_\beta = \frac{1+70\chi_\omega}{1+80\chi_\omega} \tag{A.33}$$

$$\chi_\omega = \left| \frac{\Omega_{ij}\,\Omega_{jk}\,S_{ki}}{\left(\beta_\infty^{*}\,\omega\right)^3} \right| \tag{A.34}$$

$$\Omega_{ij} = \frac{1}{2}\left(\frac{\partial u_i}{\partial x_j} - \frac{\partial u_j}{\partial x_i} \right) \tag{A.35}$$

The strain rate tensor, S_{ij} is defined as

$$S_{ij} = \frac{1}{2}\left(\frac{\partial u_j}{\partial x_i} + \frac{\partial u_i}{\partial x_j} \right) \tag{A.36}$$

and

$$\beta = \beta_i \left[1 - \frac{\beta_i^{*}}{\beta_i} \xi^{*} F(M_t) \right] \tag{A.37}$$

where β_i is defined by Equation A.28, and $F(M_t)$ is given by

$$F(M_t) = \begin{cases} 0 & M_t \le M_{t0} \\ M_t^{2} - M_{t0}^{2} & M_t > M_{t0} \end{cases} \tag{A.38}$$

where

$$M_t^{2} \equiv \frac{2k}{\alpha^{2}} \tag{A.39}$$

$$M_{t0} = 0.25 \tag{A.40}$$

$$\alpha = \sqrt{\gamma R T} \tag{A.41}$$

In the high-Reynolds-number form of the k-ω model, $\beta_i^{*} = \beta_\infty^{*}$. In the incompressible form, $\beta^{*} = \beta_i^{*}$. Model constant are given as:

$$\alpha_\infty^{*} = 1,\ \alpha_\infty = 0.52,\ \alpha_0 = \frac{1}{9},\ \beta_\infty^{*} = 0.09,\ \beta_i = 0.072,\ R_\beta = 8 \tag{A.42}$$

$$R_k = 6,\ R_\omega = 2.95,\ \xi^* = 1.5,\ M_{t0} = 0.25,\ \sigma_k = 2.0,\ \sigma_\omega = 2.0 \tag{A.43}$$

S_k and S_ω are user-defined source terms.

A.3. The Reynolds Stress Model (RSM)

In the RSM model, the individual Reynolds stresses, $\overline{u_i' u_j'}$, are calculated using differential transport equations. Closure of the Reynolds-averaged momentum equation is obtained by these individual Reynolds stresses.

A.3.1. RSM Equations

The exact transport equations for the transport of the Reynolds stresses, $\overline{u_i' u_j'}$, may be written as follows:

$$\underbrace{\frac{\partial}{\partial t}\left(\rho\overline{u_i' u_j'}\right)}_{Local\,Time\,Derivative} + \underbrace{\frac{\partial}{\partial x_k}\left(\rho u_k \overline{u_i' u_j'}\right)}_{C_{ij} \equiv Convection} = \underbrace{-\frac{\partial}{\partial x_k}\left[\rho\overline{u_i' u_j' u_k'} + \overline{p\left(\delta_{kj} u_i' + \delta_{ik} u_j'\right)}\right]}_{DT.ij \equiv Turbulent\ \ Diffusion}$$

$$+ \underbrace{\frac{\partial}{\partial x_k}\left[\mu\frac{\partial}{\partial x_k}\left(\overline{u_i' u_j'}\right)\right]}_{DL,ij \equiv Molecular\ \ Diffusion} \underbrace{-\rho\left(\overline{u_i' u_k'}\frac{\partial u_j}{\partial x_k} + \overline{u_j' u_k'}\frac{\partial u_i}{\partial x_k}\right)}_{Pij \equiv Stress\ \ Production} \underbrace{-\rho\beta\left(g_i\overline{u_j'\theta} + g_j\overline{u_i'\theta}\right)}_{Gij \equiv Buoyancy\ \ Production}$$

$$+ \underbrace{\overline{\frac{\partial u_i'}{\partial x_j} + \frac{\partial u_j'}{\partial x_i}}}_{\phi ij \equiv Pressure\ \ Strain} \underbrace{- 2\mu\overline{\frac{\partial u_i'}{\partial x_k}\frac{\partial u_j'}{\partial x_k}}}_{\varepsilon ij \equiv Dissipation}$$

$$\underbrace{-2\rho\Omega_k\left(\overline{u_j' u_m'}\varepsilon_{ikm} + \overline{u_i' u_m'}\varepsilon_{jkm}\right)}_{Fij \equiv \mathrm{Production\ \ by\ \ System\ \ Rotation}} + \underbrace{S_{user}}_{User-Defined\ Source\ Term} \tag{A.44}$$

In the above equation, the terms $D_{T,ij}$, G_{ij},Φ_{ij},and ε_{ij} must be modeled in order to close equations, while C_{ij}, $D_{L,ij}$, P_{ij}, and F_{ij} do not.

$D_{T,ij}$ is given by:

$$D_{T,ij} = \frac{\partial}{\partial x_k}\left(\frac{\mu_t}{\sigma_k}\frac{\partial \overline{u_i' u_j'}}{\partial x_k}\right) \tag{A.45}$$

where σ_k = 0.82, applying the generalized gradient-diffusion model, and

$$\mu_t = \rho C_\mu \frac{k^2}{\varepsilon} \quad \text{where} \quad C_\mu = 0.09. \tag{A.46}$$

The classical approach to modeling Φ_{ij} uses the following decomposition:

$$\phi_{ij} = \phi_{ij,1} + \phi_{ij,2} + \phi_{ij,\omega} \tag{A.47}$$

where $\phi_{ij,1}$ is the slow pressure-strain term, also known as the return-to-isotropy term, $\phi_{ij,2}$ is called the rapid pressure-strain term, and $\phi_{ij,\omega}$ is the wall-reflection term. The slow pressure-strain term, $\phi_{ij,1}$, is modeled as

$$\phi_{ij,1} = -C_1 \rho \frac{\varepsilon}{k}\left[\overline{u_i' u_j'} - \frac{2}{3}\delta_{ij} k\right] \quad \text{with } C_1 = 1.8 \tag{A.48}$$

The rapid pressure-strain term, $\phi_{ij,2}$, is modeled as

$$\phi_{ij,2} = -C_2\left[\left(P_{ij} + F_{ij} + G_{ij} - C_{ij}\right) - \frac{2}{3}\left(P + G - C\right)\right] \tag{A.49}$$

where C_2 = 0.60, P_{ij}, F_{ij}, G_{ij}, and C_{ij} are defined as in Equation A.44,

$P = \frac{1}{2}P_{kk}$, $G = \frac{1}{2}G_{kk}$, and $C = \frac{1}{2}C_{kk}$.

The wall-reflection term, $\phi_{ij,\omega}$, is responsible for the redistribution of normal stresses near the wall. It tends to damp the normal stress perpendicular to the wall, while enhancing the stresses parallel to the wall. This term is modeled as

$$\phi_{ij,\omega} = C_1' \frac{\varepsilon}{k}\left(\overline{u_k' u_m'} n_k n_m \delta_{ij} - \frac{3}{2}\overline{u_j' u_k'} n_j n_k - \frac{3}{2}\overline{u_j' u_k'} n_i n_k\right)\frac{k^{3/2}}{C_l \varepsilon d} \tag{A.50}$$

$$+ C_2'\left(\phi_{km,2}n_k n_m \delta_{ij} - \frac{3}{2}\phi_{ik,2}n_j n_k - \frac{3}{2}\phi_{jk,2}n_i n_k\right)\frac{k^{3/2}}{C_l \varepsilon d} \quad \text{(A.51)}$$

where C_1'= 0.5, C_2' = 0.3, n_k is the x_k th component of the unit normal to the wall, d is the normal distance to the wall, and $C_l = C_\mu^{3/4}/\kappa$, where C_μ = 0.09 and κ is the von Karman constant (= 0.4187).

When the enhanced wall treatment is used in RSM, the pressure strain model is modified by FLUENT specifying the values of C_1, C_2, C_1' and C_2' as functions of the Reynolds stress invariants and the turbulent Reynolds number, where

$$C_1 = 1 + 2.58A\sqrt{A_2}\left\{1 - exp\left[-\left(0.0067 Re_t\right)^2\right]\right\} \quad \text{(A.52)}$$

$$C_2 = 0.75\sqrt{A} \quad \text{(A.53)}$$

$$C_1' = -\frac{2}{3}C_1 + 1.67 \quad \text{(A.54)}$$

$$C_2' = max\left[\frac{\frac{2}{3}C_2 - 1.6}{C_2}, 0\right] \quad \text{(A.55)}$$

with the turbulent Reynolds number defined as $\mathrm{Re}_t = \left(\rho k^2/\mu\varepsilon\right)$. The parameter A and tensor invariants, A_2 and A_3, are defined as

$$A \equiv \left[1 - \frac{9}{8}\left(A_2 - A_3\right)\right] \quad \text{(A.56)}$$

$$A_2 = \alpha_{ik}\alpha_{ki} \quad \text{(A.57)}$$

$$A_3 = \alpha_{ik}\alpha_{kj}\alpha_{ji} \quad \text{(A.58)}$$

α_{ij} is the Reynolds-stress anisotropy tensor, defined as

$$a_{ij} = -\left(\frac{-\rho\overline{u_i' u_j'} + \frac{2}{3}\rho k \delta_{ij}}{\rho k} \right) \tag{A.59}$$

The production terms due to buoyancy are modeled as

$$G_{ij} = \beta \frac{\mu_t}{Pr_t}\left(g_i \frac{\partial T}{\partial x_j} + g_j \frac{\partial T}{\partial x_i} \right) \tag{A.60}$$

where Pr_t is the turbulent Prandtl number for energy, with a default value of 0.85.

In general, when the turbulence kinetic energy is needed for modeling a specific term, it is obtained by taking the trace of the Reynolds stress tensor:

$$k = \frac{1}{2}\overline{u_i' u_i'} \tag{A.61}$$

In Fluent, the following model equation is used to solve a transport equation for the turbulence kinetic energy in order to obtain boundary conditions for the Reynolds stresses:

$$\begin{aligned} &\frac{\partial}{\partial t}(\rho k) + \frac{\partial}{\partial x_i}(\rho k u_i) = \\ &\quad \frac{\partial}{\partial x_j}\left[\left(\mu + \frac{\mu_t}{\sigma_k} \right) \frac{\partial k}{\partial x_j} \right] + \frac{1}{2}(P_{ii} + G_{ii}) - \rho\varepsilon\left(1 + 2M_t^2\right) + S_k \end{aligned} \tag{A.62}$$

where σ_k = 0.82 and S_k is a user-defined source term. Although Equation A.62 is solved globally throughout the flow domain, the values of k obtained are used only for boundary conditions. In every other case, k is obtained from Equation A.61.

The dissipation tensor, ε_{ij} , is modeled as

$$\varepsilon_{ij} = \frac{2}{3}\delta_{ij}\left(\rho\varepsilon + Y_M \right) \tag{A.63}$$

where $Y_M = 2\rho\varepsilon M_t^2$ is an additional dilatation dissipation term. The turbulent Mach number in this term is defined as

$$M_t = \sqrt{\frac{k}{a^2}} \tag{A.64}$$

where $a = \sqrt{\gamma RT}$ is the speed of sound. This compressibility modification always takes effect when the compressible form of the ideal gas law is used. The scalar dissipation rate, ε, is computed by the transport equation given by

$$\frac{\partial}{\partial t}(\rho\varepsilon) + \frac{\partial}{\partial x_i}(\rho\varepsilon u_i) = \frac{\partial}{\partial x_j}\left[\left(\mu + \frac{\mu_t}{\sigma_\varepsilon}\right)\frac{\partial \varepsilon}{\partial x_j}\right] C_{\varepsilon 1}\frac{1}{2}\left[P_{ii} + C_{\varepsilon 3}G_{ii}\right]\frac{\varepsilon}{k} - C_{\varepsilon 2}\rho\frac{\varepsilon^2}{k} + S_\varepsilon \tag{A.65}$$

where σ_ε =1.0, $C_{\varepsilon 1}$ = 1.44, $C_{\varepsilon 2}$ = 1.92, $C_{\varepsilon 3}$ is evaluated as a function of the local flow direction relative to the gravitational vector, and S_ε is user defined source term. The turbulent viscosity, μ_t , is computed similarly to the k-ε models:

$$\mu_t = \rho C_\mu \frac{k^2}{\varepsilon} \tag{A.66}$$

where C_μ = 0.09.

A.3.2. Boundary Conditions for the Reynolds Stresses

At walls, FLUENT computes the near-wall values of the Reynolds stresses and ε from wall functions. FLUENT applies explicit wall boundary conditions for the Reynolds stresses by using the log-law and the assumption of equilibrium, disregarding convection and diffusion in the transport equations for the stresses (Equation A.61). Using a local coordinate system, where τ is the tangential coordinate, η is the normal coordinate, and λ is the binormal coordinate, the Reynolds stresses at the wall-adjacent cells are computed from

$$\frac{\overline{u_\tau'^2}}{k} = 1.098,\ \frac{\overline{u_\eta'^2}}{k} = 0.247,\ \frac{\overline{u_\lambda'^2}}{k} = 0.655,\ -\frac{\overline{u_\tau' u_\eta'}}{k} = 0.255 \tag{A.67}$$

To obtain k, FLUENT solves the transport equation of Equation A.62. For reasons of computational convenience, the equation is solved globally, even though the values of k thus computed are needed only near the wall; in the far field k is obtained directly from the normal Reynolds stresses using Equation A.61. By default, the values of the Reynolds stresses near the wall are fixed using the values computed from Equation A.67, and the transport equations in Equation 2.48 are solved only in the bulk flow region.

A.3.3. Convective Heat Transfer Modeling in RSM

With RSM in FLUENT, turbulent heat transport is modeled using the concept of Reynolds' analogy to turbulent momentum transfer. Thus energy equation is given by the following:

$$\frac{\partial}{\partial t}(\rho E) + \frac{\partial}{\partial x_i}\left[u_i(\rho E + p)\right] = \frac{\partial}{\partial x_j}\left[\left(k + \frac{c_p \mu_t}{Pr_t}\right)\frac{\partial T}{\partial x_j} + u_i(\tau_{ij})_{eff}\right] + S_h \tag{A.68}$$

where E is the total energy and $(\tau_{ij})_{eff}$ is the deviatoric stress tensor, defined as

$$(\tau_{ij})_{eff} = \mu_{eff}\left(\frac{\partial u_j}{\partial x_i} + \frac{\partial u_i}{\partial x_j}\right) - \frac{2}{3}\mu_{eff}\frac{\partial u_i}{\partial x_i}\delta_{ij} \tag{A.69}$$

The term involving $(\tau_{ij})_{eff}$ represents the viscous heating, and is always computed in the coupled solvers. The default value of the turbulent Prandtl number is 0.85.

A.4. Near-Wall Treatments

In turbulent flows, the mean velocity field is significantly affected through the wall no-slip condition that has to be satisfied at walls. However, the turbulence is also changed by the presence of the wall in non-trivial ways. Very close to the wall,

viscous damping reduces the tangential velocity fluctuations, while kinematic blocking reduces the normal fluctuations.

The near wall modeling is an important consideration since the walls re the main source of mean vorticity and turbulence. In the near wall region, the solution variables have large gradients and modeling this region determines the success of wall bounded turbulent flows. If the near-wall mesh resolution is sufficient, the Spalart-Allmaras, and k-ω models valid throughout the whole flow region while special treatment is needed in k-ε, RSM, and LES models that are primarily for turbulent core flows.

The near-wall flow region can be classified into three regions from wall to inner-part as viscous sub-layer in which the flow can said to be laminar and molecular viscosity dominates in momentum and heat transfer, the buffer region where effects of molecular and viscosity and turbulence nearly equal to each other, and finally the fully turbulent core region where turbulence plays a major role, respectively.

Two traditional approaches are available in modeling the near-wall region, one of in which viscous and buffer region is not resolved instead semi-empirical formulas, that is wall-function, is used, and in the second approach turbulence model is modified to enable viscosity-affected (viscous and buffer) region to be resolved with a mesh all the way to the wall, called as near-wall modeling.

In wall function approach, the solution is easier in high-Reynolds-flows since the viscosity–affected region where the solution variables rapidly change need not to be resolved. This method is popular because it is economical, robust, reasonably accurate, and practical option for industrial flow simulations. However, it is inadequate in dominant low-Reynolds-number flows since it loses its validity. FLUENT offers two choices of standard and two-layer non-equilibrium wall functions comprising laws-of-the-wall for mean velocity and temperature (or other scalars), and formulas for near-wall turbulent quantities. It also presents another option, enhanced wall treatment, which is a near-wall modeling method including a two-layer model with enhanced wall functions [FLUENT ug, 2006].

APPENDIX-B : Lateral Velocity Vectors in Grid Spacer Region

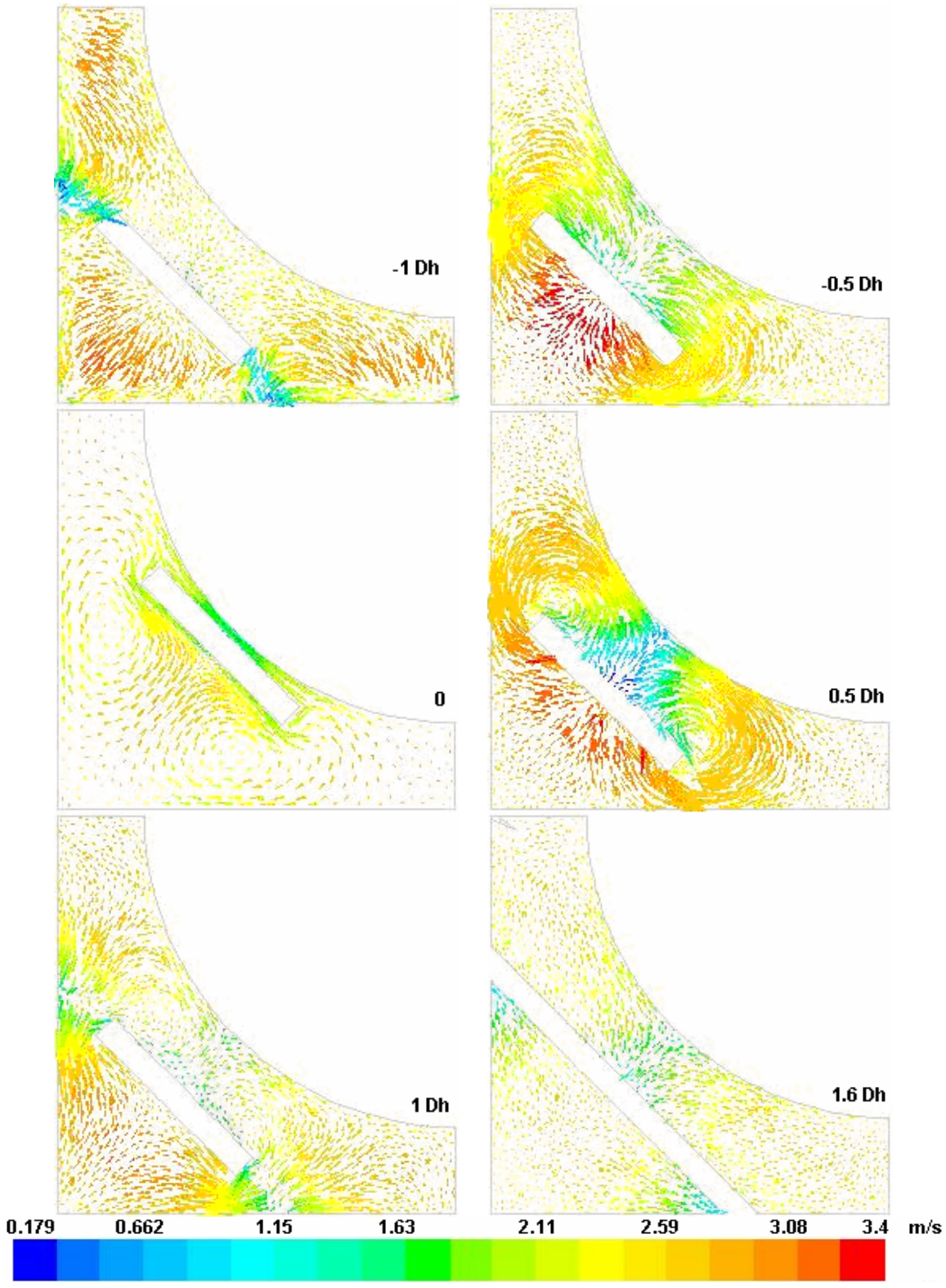

Figure B.1. Lateral velocity vectors, case-1(st. k-ε, enhanced wall treatment)

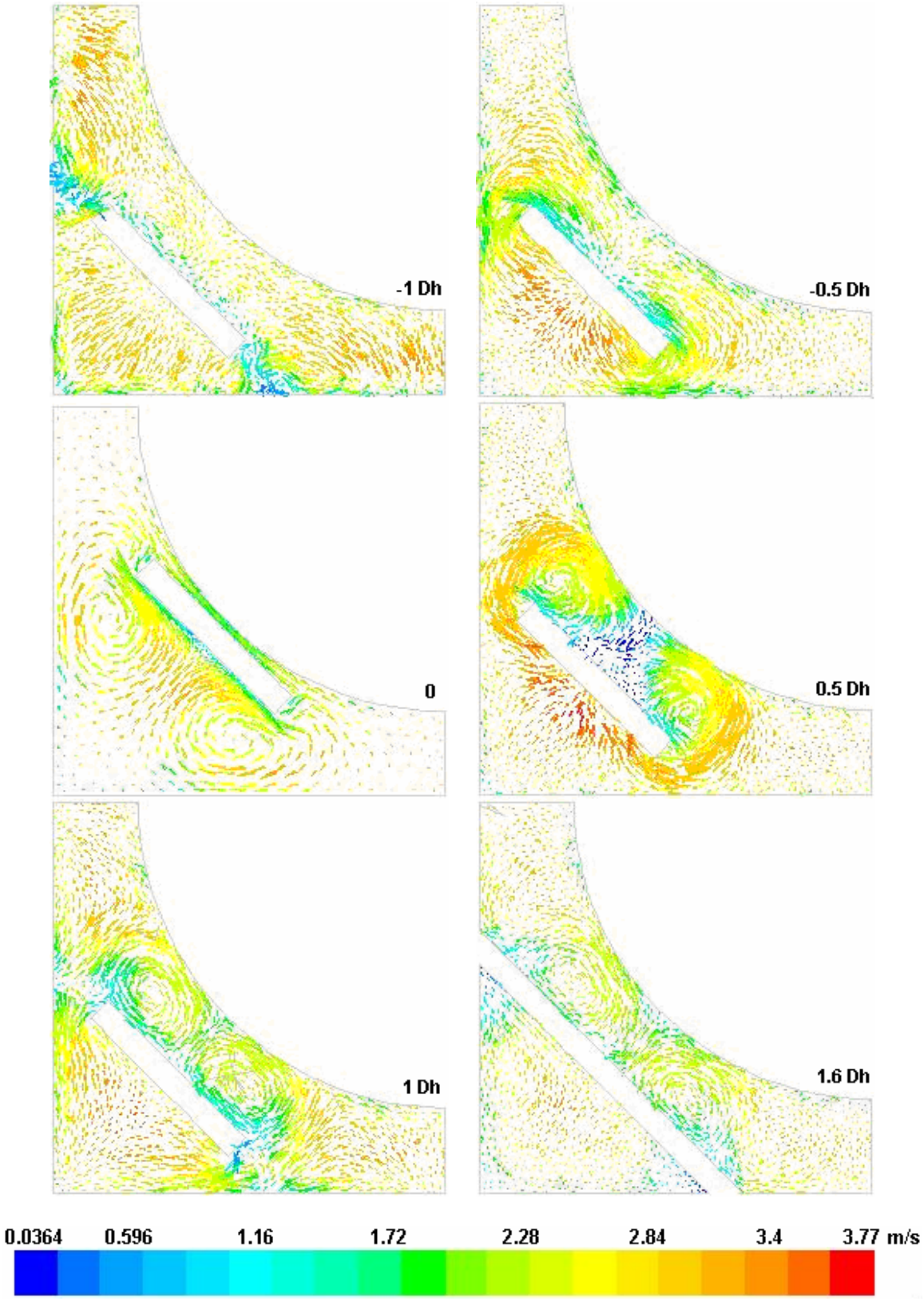

Figure B.2. Lateral velocity vectors, case-3(st. k-ω, enhanced wall treatment)

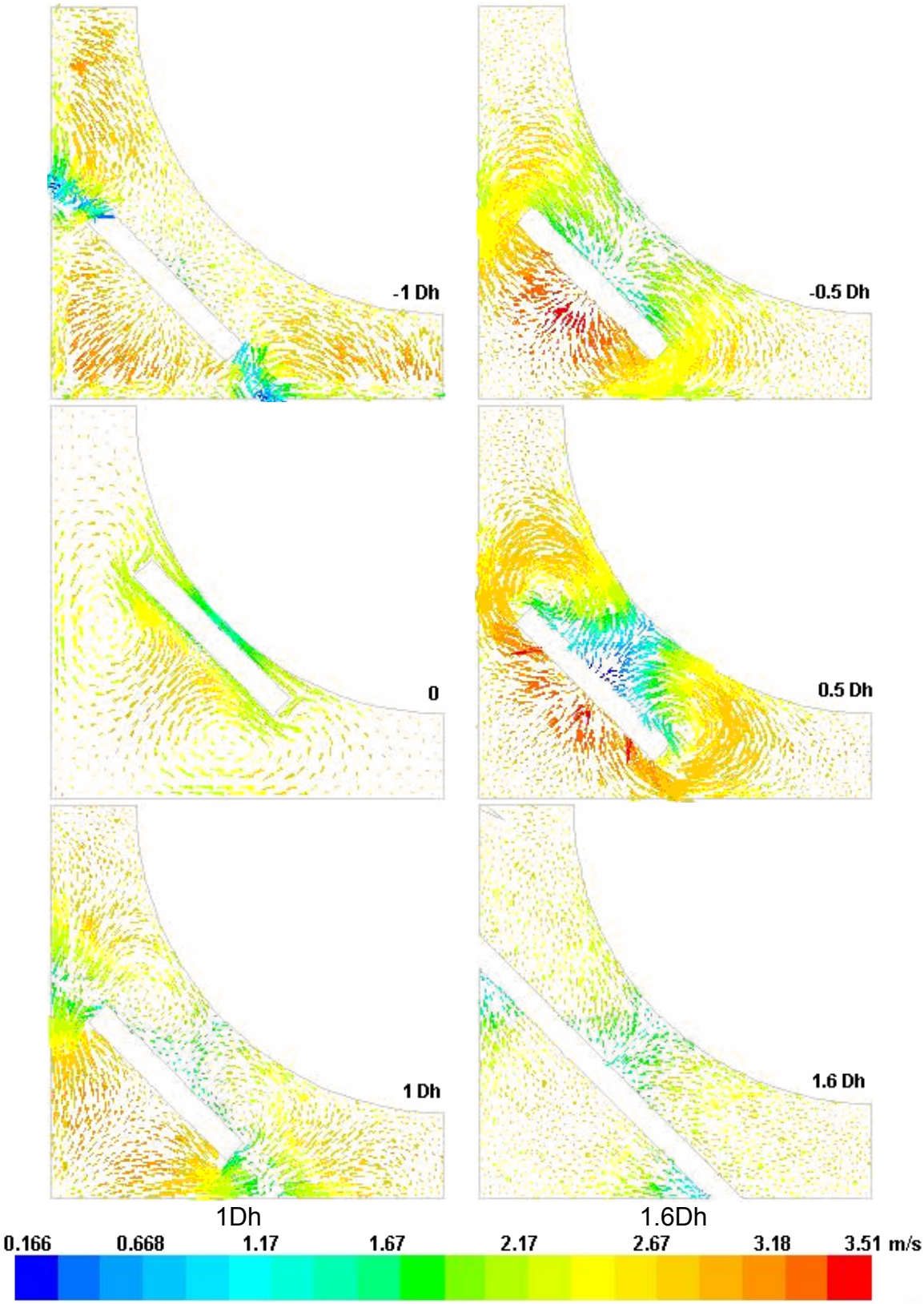

Figure B.3. Lateral velocity vectors, case-3(RSM, enhanced wall treatment)

APPENDIX-C: Lateral Velocity Vectors Downstream of grid and ferrule spacer

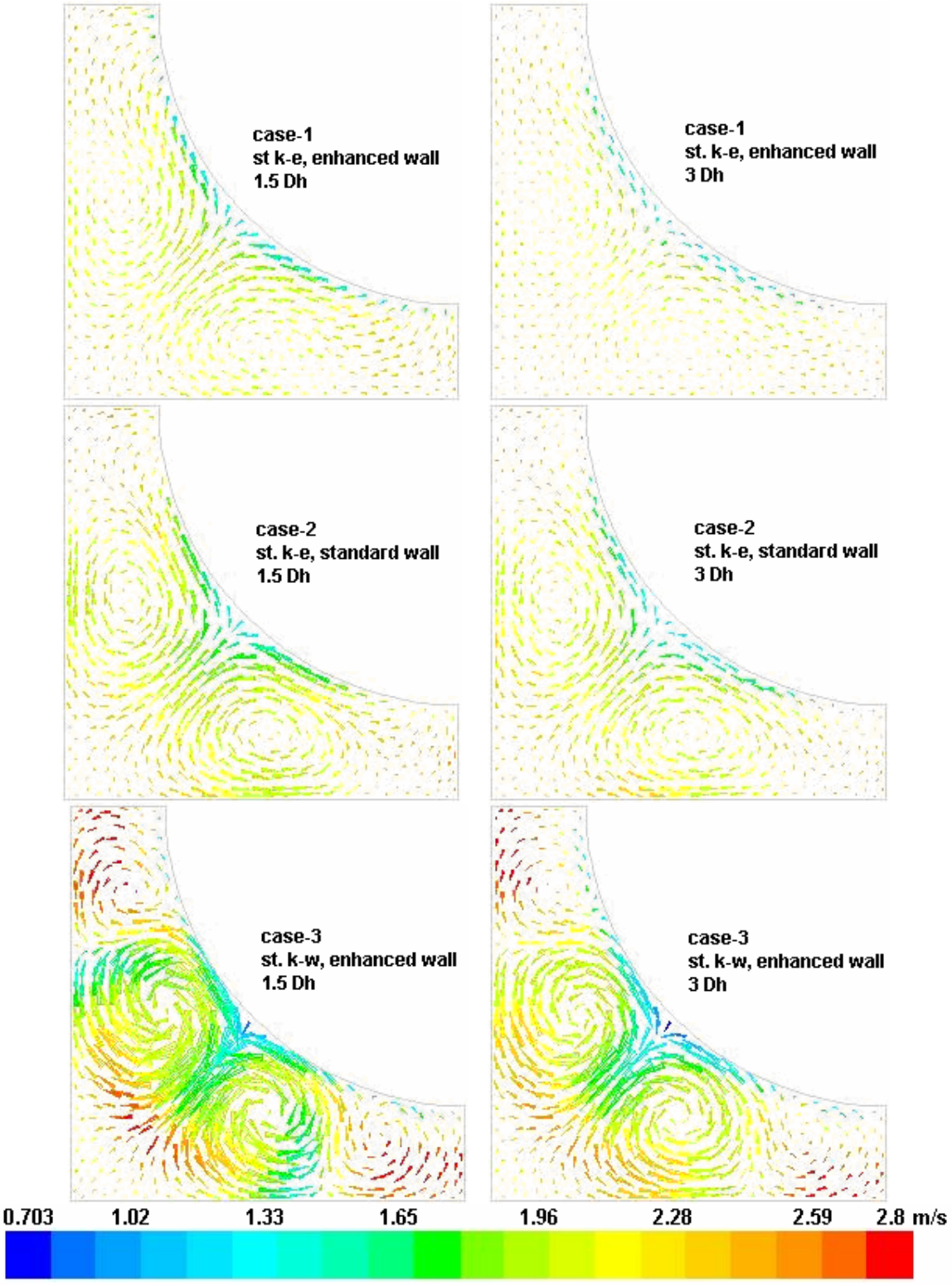

Figure C.1. Lateral velocity vectors downstream of grid spacer (continued)

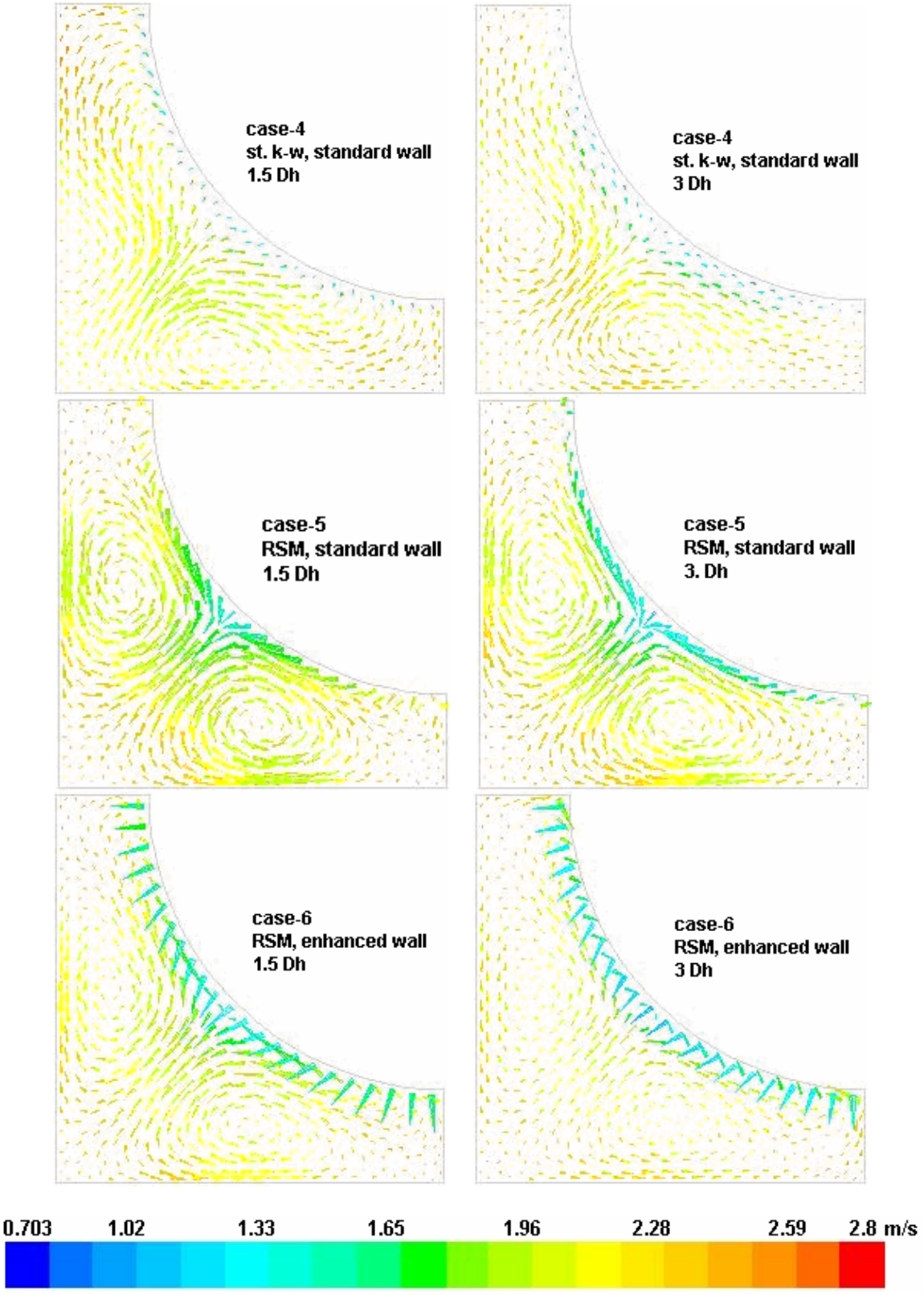

Figure C.1. Lateral velocity vectors downstream of grid spacer

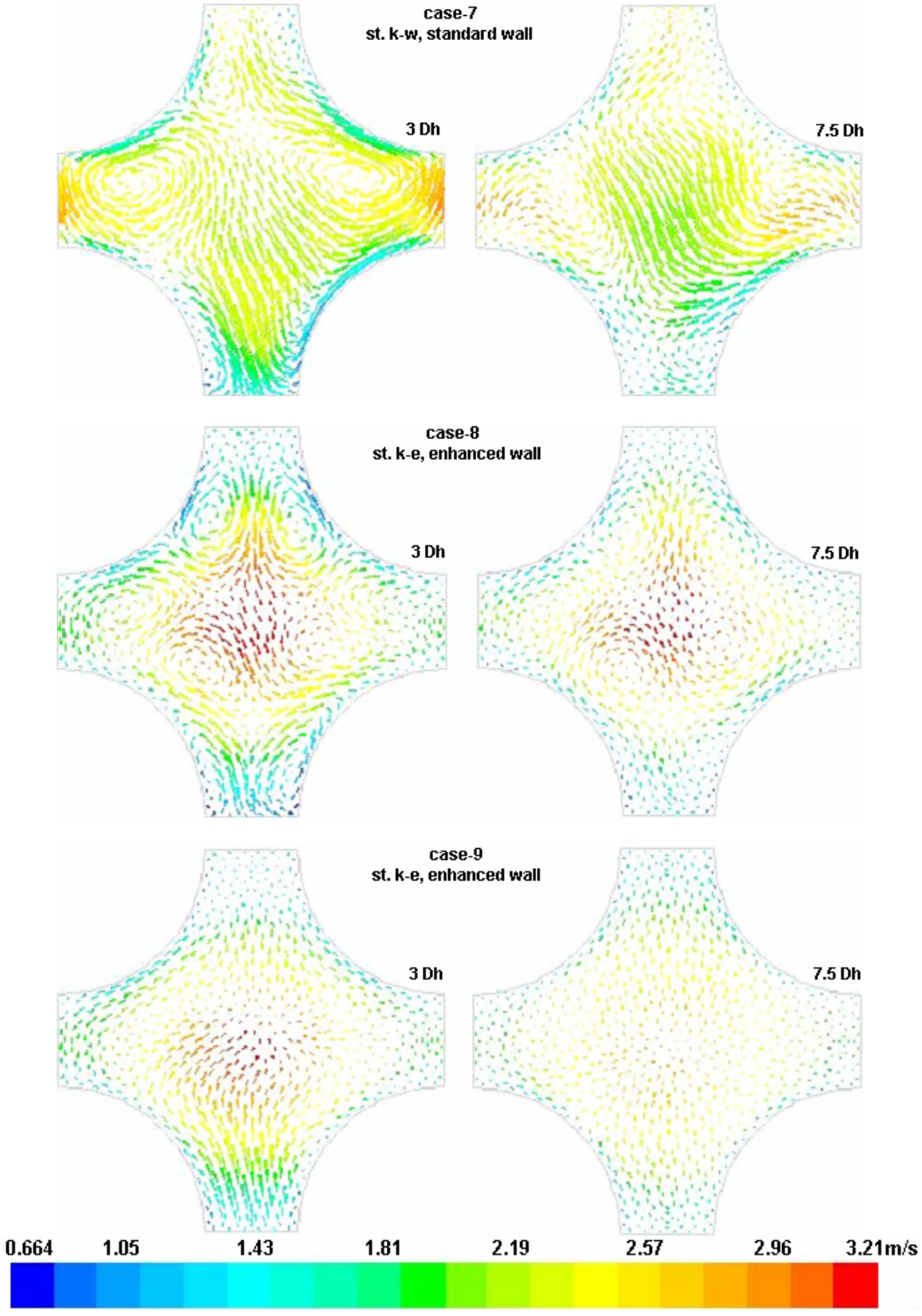

Figure C.2. Lateral velocity vectors downstream of ferrule spacer (continued)

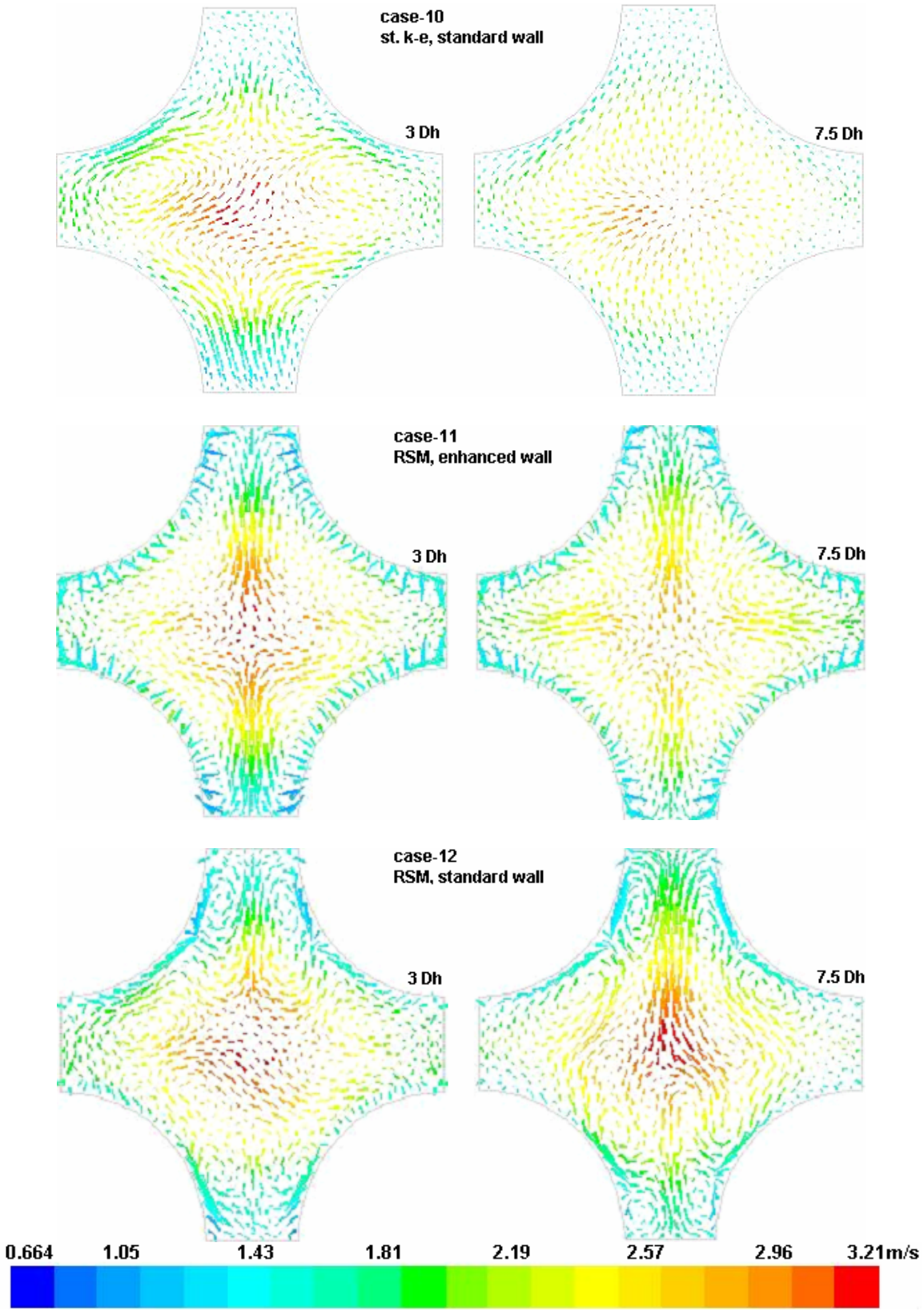

Figure C.2. Lateral velocity vectors downstream of ferrule spacer

APPENDIX-D
User-defined function coded in C language, for TKE and TDR source terms.

```
#include "udf.h"
DEFINE_SOURCE(tke_source, c1, t1, dS, eqn)
{
real k_source;
real pos[ND_ND];
C_CENTROID(pos,c1,t1);
if (pos[2] >= -0.02435 && pos[2] <= 0.02435)
{
/* source term */
k_source =
1650.0*pow(sqrt(pow(C_U(c1,t1),2)+pow(C_V(c1,t1),2)+pow(C_W(c1,t1),2)),3);
}
else
k_source = 0.;
return k_source;
}

DEFINE_SOURCE(eps_source, c, t, dS, eqn)
{
real e_source;
real sk;
real pos[ND_ND];
C_CENTROID(pos,c,t);
if (pos[2] >= -0.02435 && pos[2] <= 0.02435)
{
/* source term */
sk = 1650.0*pow(sqrt(pow(C_U(c,t),2)+pow(C_V(c,t),2)+pow(C_W(c,t),2)),3);
e_source = 1.44*C_D(c,t)*sk/C_K(c,t);
}
else
e_source = 0.;
return e_source;
}
```